



# Preclinical evaluation of a brain penetrant PARP PET imaging probe in rat glioblastoma and nonhuman primates

Baosheng Chen<sup>1</sup> · Devi Prasan Ojha<sup>1</sup> · Takuya Toyonaga<sup>1</sup> · Jie Tong<sup>1</sup> · Richard Pracitto<sup>1</sup> · Monique A. Thomas<sup>2</sup> · Michael Liu<sup>1</sup> · Michael Kapinos<sup>1</sup> · Li Zhang<sup>1</sup> · Ming-Qiang Zheng<sup>1</sup> · Daniel Holden<sup>1</sup> · Krista Fowles<sup>1</sup> · Jim Ropchan<sup>1</sup> · Nabeel Nabulsi<sup>1</sup> · Henk De Feyter<sup>2</sup> · Richard E. Carson<sup>1</sup> · Yiyun Huang<sup>1</sup> · Zhengxin Cai<sup>1</sup>

Received: 3 October 2022 / Accepted: 18 February 2023 / Published online: 28 February 2023  
© The Author(s), under exclusive licence to Springer-Verlag GmbH Germany, part of Springer Nature 2023

## Abstract

**Purpose** Currently, there are multiple active clinical trials involving poly(ADP-ribose) polymerase (PARP) inhibitors in the treatment of glioblastoma. The noninvasive quantification of baseline PARP expression using positron emission tomography (PET) may provide prognostic information and lead to more precise treatment. Due to the lack of brain-penetrant PARP imaging agents, the reliable and accurate *in vivo* quantification of PARP in the brain remains elusive. Herein, we report the synthesis of a brain-penetrant PARP PET tracer, (*R*)-2-(2-methyl-1-(methyl-<sup>11</sup>C)pyrrolidin-2-yl)-1*H*-benzo[*d*]imidazole-4-carboxamide (<sup>11</sup>C]PyBic), and its preclinical evaluations in a syngeneic RG2 rat glioblastoma model and healthy nonhuman primates.

**Methods** We synthesized [<sup>11</sup>C]PyBic using veliparib as the labeling precursor, performed dynamic PET scans on RG2 tumor-bearing rats and calculated the distribution volume ratio (DVR) using simplified reference region method 2 (SRTM2) with the contralateral nontumor brain region as the reference region. We performed biodistribution studies, western blot, and immunostaining studies to validate the *in vivo* PET quantification results. We characterized the brain kinetics and binding specificity of [<sup>11</sup>C]PyBic in nonhuman primates on FOCUS220 scanner and calculated the volume of distribution ( $V_T$ ), nondisplaceable volume of distribution ( $V_{ND}$ ), and nondisplaceable binding potential ( $BP_{ND}$ ) in selected brain regions.

**Results** [<sup>11</sup>C]PyBic was synthesized efficiently in one step, with greater than 97% radiochemical and chemical purity and molar activity of  $148 \pm 85$  MBq/nmol ( $n = 6$ ). [<sup>11</sup>C]PyBic demonstrated PARP-specific binding in RG2 tumors, with 74% of tracer binding in tumors blocked by preinjected veliparib (*i.v.*, 5 mg/kg). The *in vivo* PET imaging results were corroborated by *ex vivo* biodistribution, PARP1 immunohistochemistry and immunoblotting data. Furthermore, brain penetration of [<sup>11</sup>C]PyBic was confirmed by quantitative monkey brain PET, which showed high specific uptake ( $BP_{ND} > 3$ ) and low nonspecific uptake ( $V_{ND} < 3$  mL/cm<sup>3</sup>) in the monkey brain.

**Conclusion** [<sup>11</sup>C]PyBic is the first brain-penetrant PARP PET tracer validated in a rat glioblastoma model and healthy nonhuman primates. The brain kinetics of [<sup>11</sup>C]PyBic are suitable for noninvasive quantification of available PARP binding in the brain, which posits [<sup>11</sup>C]PyBic to have broad applications in oncology and neuroimaging.

**Keywords** Glioblastoma · PARP · Brain PET · RG2 · Nonhuman primate · Cerebellum · Hippocampus

## Abbreviations

BBB Blood brain barrier  
PARP Poly (ADP-ribose) polymerase  
GBM Glioblastoma multiforme

SUV Standardized uptake value  
TAC Time activity curve  
RCY Radiochemical yield  
PDB Protein database  
HPLC High-performance liquid chromatography

This article is part of the Topical Collection on Oncology - Brain.

Baosheng Chen, Devi Prasan Ojha, Takuya Toyonaga, Jie Tong are authors contributed equally.

✉ Zhengxin Cai  
Jason.cai@yale.edu

Extended author information available on the last page of the article

## Introduction

The enzyme poly(ADP-ribose) polymerase-1 (PARP1) is one of 17 members in the PARP family and is involved in the base excision repair (BER) pathway that regulates DNA single-strand break (SSB) repair [1, 2]. PARP1 is the

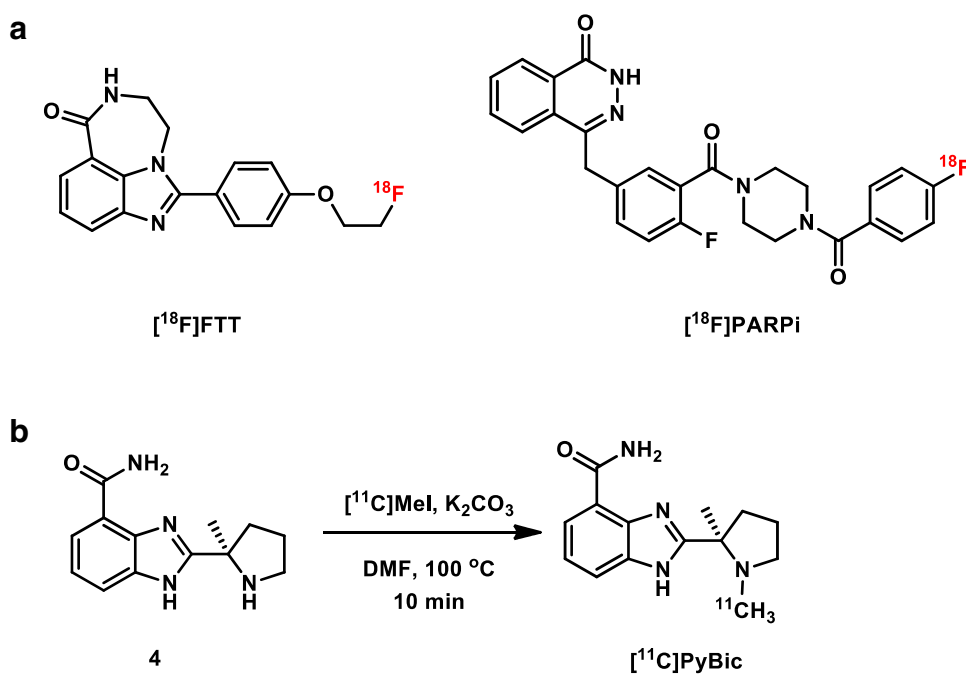
most abundant PARP member and accounts for 90% of the NAD<sup>+</sup> used by the PARP family to catalyze poly(ADP-ribose) on proteins and oligonucleotides. DNA damage activates PARP1 towards addition with ADP-ribose, forming a polymeric, energy rich scaffold of poly(ADP-ribose) (PAR), which is an essential energy source in DNA SSB and BER. The process of DNA repair can be interrupted by PARP inhibition, which leads to the accumulation of DNA SSBs and results in synthetic lethality in cancer cells with BRCA1/2 mutations [3]. Thus, PARP inhibitors (PARPis) are actively pursued as treatments for a variety of cancers, including ovarian, breast and brain tumors. To date, the FDA has approved four PARPis for the treatment of ovarian cancer and breast cancer, *i.e.*, olaparib (AZD2281), niraparib, rucaparib and talazoparib.

Malignant gliomas are highly aggressive tumors with poor prognosis, among which glioblastoma (GBM) is the most aggressive. Even with the intensive regimen of surgical removal followed by radio/chemotherapy, the 5-year survival rate is only 5% for GBM patients [4]. The rapid infiltration of tumor cells into surrounding tissues limits the complete surgical excision of GBM tumors. The complex neurovascular physiology of the blood–brain barrier (BBB) and blood-tumor barrier (BTB) limits the penetration and distribution of some therapeutic drugs [5]. The nature of tumor heterogeneity that contributes to the development of resistance to therapies and the active efflux of small molecule drugs are among the major challenges in finding a cure for malignant gliomas [6–8].

PARP1 is overexpressed in GBM, and its levels positively correlated with tumor grades in gliomas, such as

proneural and classical GBM subtypes [9]. Thus, *in vivo* assessment of PARP1 expression levels could assist in the identification of glioma subtypes and provide prognostic value in guiding treatment options. However, there is currently no reported method to quantify PARP1 expression levels in the brain. PET imaging allows for noninvasive whole-body quantification of protein expression and has been used to delineate tumors [10], provide functional information [11], predict patient response to a targeted therapy, assess therapeutic effects [12–16], and provide a global and dynamic picture of the disease biomarkers in primary tumors and metastatic sites [17]. Therefore, PET imaging with PARP1 radioligands could allow for the *in vivo* quantification of PARP1 expression for patient stratification, assessing target engagement by PARPis, and monitoring treatment effects. Great efforts have been devoted to developing PARP PET imaging probes using the potent PARPis olaparib and rucaparib and, more recently, talazoparib as the lead compounds, culminating in the translation of [<sup>18</sup>F]FTT and [<sup>18</sup>F]PARPi into human studies (Fig. 1a) [18, 19]. However, veliparib has been essentially overlooked as a leading compound for PARP PET tracer development, despite its more desirable characteristics for brain PET imaging, *i.e.*, high brain exposure, fast brain kinetics and less P-glycoprotein (P-gp) efflux from the brain [20]. As a therapeutic drug, veliparib has been investigated extensively to treat non-small cell lung cancer, BRCA-mutated advanced breast cancer and ovarian cancer [21–24]. In fact, some of the current PARP PET tracers have been investigated as PET imaging agents in gliomas but suffer from limited brain penetration and

**Fig. 1** (a) PARP PET tracers derived from the PARP1/2 inhibitors olaparib and rucaparib. (b) Radiochemical synthesis of [<sup>11</sup>C]PyBic



liability to efflux by transporter proteins [25, 26]. Using veliparib as the lead, we performed computational analysis, identified and synthesized an *N*-<sup>11</sup>C-methylated veliparib derivative, (*R*)-2-(2-methyl-1-(methyl-<sup>11</sup>C)pyrrolidin-2-yl)-1*H*-benzo[*d*]imidazole-4-carboxamide ([<sup>11</sup>C]PyBic), based on its predicted desirable physicochemical properties as a brain penetrant PET tracer, and evaluated its potential to image and quantify PARP in GBM and healthy brains. Specifically, we tested the *in vivo* specific binding signals of [<sup>11</sup>C]PyBic in a rodent GBM model through baseline and blocking studies. *Ex vivo* metabolite analysis showed no substantive radiometabolites in healthy rat brains. PET imaging results were corroborated by *ex vivo* biodistribution of [<sup>11</sup>C]PyBic, western blotting and immunohistochemical staining of PARP1 in selected brain regions and the implanted tumors. Furthermore, we confirmed the BBB penetration of [<sup>11</sup>C]PyBic using quantitative nonhuman primate (NHP) brain PET imaging [20, 27, 28]. Blocking studies with the structurally analogous veliparib and the structurally distinctive PARPi BGB290 (Pamiparib) [29] confirmed PARP-specific tracer uptake in NHP brains.

## Materials and methods

### Chemicals

All reagents and solvents were purchased from commercial sources (Sigma-Aldrich, VWR, and Fisher Scientific) and used without further purification. The tritium-labeled PyBic, [<sup>3</sup>H]PyBic, was purchased from Novandi Cehmistry AB (Sweden) as an ethanol solution (37 MBq/mL) with a chemical and radiochemical purity of 99% and a molar activity of 3.0 TBq/mmol (NC064-04-1). <sup>1</sup>H NMR spectra were recorded on an Agilent 400 or 600 MHz spectrometer with tetramethylsilane as an internal standard. All chemical shifts ( $\delta$ ) were reported in parts per million (ppm) downfield relative to the chemical shift of tetramethylsilane. Signals were quoted as s (singlet), d (doublet), dt (double triplets), t (triplet), q (quartet), or m (multiplet). High-resolution mass spectra (HRMS) were obtained and recorded on a Thermo Scientific LTQ Orbitrap XL Elite system. The P-gp efflux assay was performed by Eurofins (MO, U.S. using a Caco-2 cell monolayer at pH 7.4.

### Computational study

Docking calculations were performed using the PARP1 cocrystallized structure of olaparib with PDB code 5DS3. The protein binding site was prepared using the protein preparation wizard (Schrodinger, New York) in Maestro. For better accuracy, water and heteroatoms > 5 Å from the active site region

were removed. The ligands were listed with tautomers and stereoisomers for the study; furthermore, geometry-optimized ligands were prepared using LigPrep wizard (Schrodinger, New York). For the docking calculations, standard-precision (SP, Schrodinger, New York) was specified for preliminary calculations, and the extra-precision (XP, Schrodinger, New York) mode was specified for the final calculations. The results were obtained from the top 70 poses obtained from Glide. Furthermore, the blood brain barrier relevant parameters, such as MDCK permeability, PSA, and logS, were also calculated based on the QikProp predictions (Schrodinger, New York).

### Synthesis of precursor and reference standard for [<sup>11</sup>C]PyBic

#### Tert-butyl (*R*)-2-(4-carbamoyl-1*H*-benzo[*d*]imidazol-2-yl)-2-methylpyrrolidine-1-carboxylate (3)

To a mixture of 2-methylimidazole (1 mmol, 1 equiv) and CDI (1.05 mmol, 1.05 equiv) was added a solution of (*R*)-1-(tert-butoxycarbonyl)-2-methylpyrrolidine-2-carboxylic acid (1, 1 mmol, 1 equiv) in NMP (1.5 mL). Consumption of the carboxylic acid derivative was monitored using TLC over 2 h. 3-Carbamoylbenzene-1,2-diaminium chloride (2, 1 mmol, 1.0 equiv) was then added to the reaction mixture. The resultant solution was stirred at 90 °C for 12 h. Anhydrous sodium acetate (2.2 mmol, 2.2 equiv) and glacial acetic acid (2.2 mmol, 2.2 equiv) were added to the reaction mixture. The mixture was refluxed for 8 h. The mixture was cooled to room temperature, poured into brine, and extracted with ethyl acetate (3 × 20 mL). The combined organic extracts were concentrated to a residue and purified by flash chromatography to obtain 3 (185 mg, 54% yield) as a colorless solid. <sup>1</sup>H NMR (400 MHz, MeOH-*D*<sub>4</sub>):  $\delta$  7.90 (dd, *J* = 8.0, 1.0 Hz, 1H), 7.63 (d, *J* = 8 Hz, 1H), 7.32–7.27 (m, 1H), 3.81–3.74 (m, 1H), 3.65–3.59 (m, 1H), 2.33–2.16 (m, 2H), 2.08–1.96 (m, 2H), 1.89 (s, 3H), 1.41 (s, 3H), 1.00 (s, 6H); <sup>13</sup>C-NMR (100 MHz, MeOH-*D*<sub>4</sub>):  $\delta$  169.0, 160.6, 154.1, 141.0, 134.8, 122.4, 121.6, 120.9, 114.7, 79.1, 42.5, 27.3, 26.7, 22.5, 22.0.

#### (*R*)-2-(2-Methylpyrrolidin-2-yl)-1*H*-benzo[*d*]imidazole-4-carboxamide (4)

Compound 3 (172 mg, 0.5 mmol, 1 equiv) was added to isopropyl alcohol (3 mL). The mixture was stirred while heating at 65 °C until the compound was dissolved. Concentrated hydrochloric acid (200  $\mu$ L, 0.25 mmol, 5 equiv) was added to this solution. The temperature was raised to 80 °C and maintained for 4 h. The mixture was then allowed to cool to room temperature. The precipitate formed was isolated, washed with *i*-PrOH (2 mL) and further dried in a vacuum oven at 50 °C to obtain 4 (70 mg, 40% yield) as a yellow solid. <sup>1</sup>H NMR (400 MHz, MeOH-*D*<sub>4</sub>): 7.90 (dd, *J* = 8.0, 1.0 Hz, 1H), 7.63 (d, *J* = 8 Hz, 1H),

7.32–7.27 (m, 1H), 3.68–3.53 (m, 2H), 2.61–2.54 (m, 1H), 2.42–2.23 (m, 2H), 2.13–2.03 (m, 2H), 1.93 (s, 3H).

### (R)-2-(1,2-dimethylpyrrolidin-2-yl)-1H-benzo[d]imidazole-4-carboxamide (5)

$K_2CO_3$  (2.5 equiv) and MeI (1.1 equiv) were added to a 50 mL flask to a solution containing 4 (30 mg) and DMF (1 mL). The reaction mixture was stirred at 100 °C for 12 h. The mixture was then allowed to cool to room temperature, poured into water (10 mL) and extracted with ethyl acetate (3 × 5 mL). The combined organic portions containing 5 were concentrated to a residue. The residue was further purified using silica gel column chromatography to afford 5 (11 mg, 56% yield) as a colorless solid.  $^1H$  NMR (400 MHz, MeOH- $D_4$ ) 7.87 (d,  $J=8.0$  Hz, 1H), 7.67 (d,  $J=8$  Hz, 1H), 7.28 (t,  $d=8.0$  Hz, 1H), 3.09–3.03 (m, 1H), 2.87–2.82 (m, 1H), 2.39–2.32 (m, 1H), 2.24 (s, 3H), 2.07–1.93 (m, 3H), 1.58 (s, 3H);  $^{13}C$ -NMR (100 MHz, MeOH- $D_4$ ) 169.2, 161.8, 159.7, 122.2, 121.4, 118.2, 115.3, 63.2, 53.3, 39.98, 34.2, 21.4, 17.5. HRMS (ESI)  $m/z$  calculated for  $C_{14}H_{19}N_4O$  [M+H]: 259.1559. Found: 259.1537.

### Radiochemistry

Solid-phase extraction (SPE) Sep-Pak cartridges were purchased from Waters Associates (Milford, MA, USA). The HPLC system used for purification of crude product included a Shimadzu LC-20A pump, a Knauer K200 UV detector, and a Bioscan  $\gamma$ -flow detector, with a Luna C18(2) semipreparative column. The HPLC system used for quality control tests was composed of a Shimadzu LC-20A pump, a Shimadzu SPD-M20A PDA or SPD-20A UV detector, and a Bioscan  $\gamma$ -flow detector, with a Gemini NX column eluting with a mobile phase of 20%  $CH_3CN$  and 80% 0.1% triethyl amine (TEA) buffer solution (pH 11.75) at a flow rate of 2 mL/min.

$[^{11}C]CO_2$  was produced through the  $^{14}N(p,\alpha)^{11}C$  nuclear reaction by bombardment of a high-pressure target containing a mixture of nitrogen and oxygen (0.5%–1%) with a 16.8-MeV proton beam that was produced by the PET Trace cyclotron (GE Healthcare) cyclotron.  $[^{11}C]MeI$  was synthesized by the gas-phase method from  $[^{11}C]CO_2$  using the FXMeI module (GE Healthcare) by initially converting  $[^{11}C]CO_2$  to  $[^{11}C]$ -methane, followed by the reaction of  $[^{11}C]$ -methane with iodine at 720 °C to produce  $[^{11}C]MeI$ .

### Experimental procedure for the radiochemical synthesis of $[^{11}C]PyBic$

After trapping  $[^{11}C]MeI$  into a reaction vial containing  $K_2CO_3$  (2.5 equiv.) and precursor 4 (1.5 mg) in DMF (0.3 mL), the reaction mixture was heated at 100 °C for 10 min. Subsequently, the mixture was quenched with

1.5 mL of 20 mM  $NH_4HCO_3$  buffer (pH=8.8) and MeCN in an 80:20 (v/v) ratio as the HPLC eluent. The mixture was eluted with the HPLC mobile phase at a flow rate of 5 mL/min. The product portion was collected using a semiPrep-HPLC setup using a Phenomenex Luna C-18 HPLC column (10  $\mu$ m, 10 mm × 250 mm) with a retention time of approximately 20 min. The product, which was collected into 50 mL of water, was then trapped on a C18 light SepPak cartridge (Waters). The cartridge was washed with 10 mL of water. The cartridge was eluted with 1 mL of ethanol and 3 mL of saline, and the radioactive material was finally collected in a dose vial precharged with 7 ml of saline and 8.4% USP sodium bicarbonate solution.

### Measurement of lipophilicity (log $D_{7.4}$ )

The lipophilicity was determined by the modified method from previously published procedures [30]. Log  $D_{7.4}$  was measured and calculated as the ratio of decay-corrected radioactivity concentrations in 1-octanol and phosphate-buffered saline (PBS, pH=7.4, Dulbecco). Six consecutive equilibrations of  $[^{11}C]PyBic$  in 1-octanol and phosphate-buffered saline (PBS, pH=7.4, Dulbecco) were performed until a constant value of log  $D_{7.4}$  was obtained.

### Saturation binding assay using $[^3H]PyBic$ in rat hippocampus and NHP brain tissue

The saturation binding assay was performed at Gifford Bioscience (UK). The hippocampus was dissected from the rat brain. The cerebellum, brain stem, frontal cortex, hippocampus, and occipital cortex were dissected from the monkey brain. The dissected brain tissues were homogenized in ice-cold buffer (50 mM Tris; 5 mM  $MgCl_2$ ; 5 mM EDTA; protease inhibitor cocktail). After a low-speed spin (100 × g) to remove tissue pieces, the supernatant was transferred to a fresh tube and centrifuged at 17,000 × g for 10 min at 4 °C to pellet the membranes. The pellet was resuspended in fresh buffer and centrifuged a second time. The pellet from the second spin was resuspended in buffer (50 mM Tris, 5 mM  $MgCl_2$ , 0.1 mM EDTA) containing 10% sucrose as a cryoprotectant, divided into aliquots, frozen, and stored at -80 °C. A sample of the washed membrane preparation was analyzed for protein content using the Pierce® BCA assay.

Radioligand binding assays were carried out in 96-well plates in a final volume of 250  $\mu$ L per well. Then, 150  $\mu$ L membrane, 50  $\mu$ L cold compound in buffer (or buffer alone) and 50  $\mu$ L radioligand in buffer were added to each well. The plate was incubated at 30 °C for 90 min with gentle agitation. The incubation was stopped by vacuum filtration onto presoaked (incubation buffer) GF/C filters using a 96-well FilterMate™ harvester, followed by five washes

with ice-cold wash buffer. Filters were then dried under a warm air stream and sealed in polyethylene, a scintillation cocktail was added, and the radioactivity was counted in a Wallac® TriLux 1450 MicroBeta counter. For each concentration of drug, nonspecific binding was subtracted from total binding to give specific binding. Data were fitted using the nonlinear curve fitting routines in Prism® (GraphPad Software Inc.) to determine  $K_d$  and  $B_{max}$ .

### Animal model

All animal procedures were approved by the Yale University Institutional Animal Care and Use Committee. The syngeneic orthotopic RG2 tumor model was established following published protocols [31] using male F344 rats (200–220 g, 10–12 weeks old) purchased from Charles River Laboratory. In short, RG2 cells (ATCC, Manassas, VA) were grown under standard cell culture conditions in T-75 flasks. Cells (~ 10,000) were suspended in sterile phosphate-buffered saline and injected into the striatum in the right hemisphere of Fischer 344 rats using a Hamilton syringe and a stereotactic device (David Kopf Instruments, Tujunga, CA). RG2 tumor growth was monitored by contrast-enhanced MR (CEMR) imaging at 14–18 days post implantation of tumor cells. The tumor volumes are from 5.8 mm<sup>3</sup> to 12.3 mm<sup>3</sup> for the 14-day post implantation cohort, from 28.9 mm<sup>3</sup> to 180.6 mm<sup>3</sup> for the 18-day post implantation cohort.

Multiple cohorts of in vivo, in vitro and ex vivo studies were performed using the same (when available) or different animals as indicated in the supplementary Table 5 and 6.

### MR imaging

RG2-bearing rats were scanned on an 11.7 T Magnex magnet (Magnex Scientific Ltd.) interfaced to a Bruker Avance III HD spectrometer running on ParaVision 6 (Bruker Instruments). Rats were anesthetized with isoflurane using a 70/30% N<sub>2</sub>O/O<sub>2</sub> mixture as the carrier gas delivered via a nose cone. Animals were positioned prone in a heated holder to maintain body temperature at 37 °C. Before positioning in the scanner, animals were injected subcutaneously with a bolus of 200 µL T1 contrast agent gadopentetate dimeglumine (Magnevist®, Bayer). For MRI acquisition, a 20 mm 1H surface coil was used, positioned directly above the animal's head. After scout images were acquired to confirm positioning, T1-weighted MR images were acquired using a multislice spin-echo pulse sequence with a repetition time of 1000 ms, echo time of 6.4 ms, isotropic resolution of 250 µm and 4 averages.

After automatic contrast adjustment of the MR images, tumor segmentation was performed using an intensity threshold and manual segmentation tools to outline the contrast-enhancing region in each slice of the MR image stack, and the segmentation results were exported.

### PET imaging experiments in glioblastoma rats and healthy rats

First, 4 RG2-bearing rats underwent a 0–90 min scan (baseline, n = 2; blocking, n = 2). Then, 5 other RG2-bearing rats underwent a 0–60 min scan (baseline, n = 3; blocking, n = 2) on FOCUS-220 scanners (Siemens Medical Solutions, Knoxville, TN, USA). [<sup>11</sup>C]PyBic (23 ± 6 MBq, 400 µL) was injected intravenously in the tail vein for both baseline and blocking scans. For blocking studies, the blocking agent veliparib (ABT-888, 5 mg/kg) was administered IV 10 min prior to the radiotracer injection. The blocking dose was prepared by dissolving 5 mg of veliparib in a solution of 1 mL of EtOH and saline in a 1:9 ratio. After the emission scan, a 9-min transmission scan was obtained for attenuation correction.

Images were reconstructed with the 3D ordered subset expectation maximization method (OSEM3D; 2 iterations, 16 subsets) with a maximum a posteriori algorithm (MAP; 25 iterations) with corrections for decay, attenuation, scatter, normalization, and randoms. The 60- and 90-min dynamic scans were reconstructed to 20 and 26 frames, respectively: 6 × 30 s, 1 × 45 s, 2 × 60 s, 1 × 90 s, 1 × 120 s, 1 × 210 s, and 10 × 300 s for 60-min scans or 15 × 300 s for 90-min scans.

An averaged PET image from 0 to 60 min for each measurement (mean of all frames) was coregistered to the T2 weighted image in the Waxholm Space rat brain atlas [32] with 6-degree-of-freedom linear registration using an in-house manual registration tool. ROIs were extracted from the atlas, and regional time-activity curves (TACs) were obtained by applying template ROIs to the PET images. Analysis included the following ROIs: cerebellum, hippocampus, neocortex, thalamus, stratum, and brain stem (BS). Tumor and contralateral nontumor ROIs were manually drawn on the individual 0–60/90 min summed PET images by referring to each individual contrast-enhanced MRI.

For P-gp inhibitor studies, PET scans were performed with (n = 1) or without (n = 2) the pre-injected P-gp inhibitor verapamil (1 mg/kg, i.v., 10 min before radiotracer injection) using [<sup>11</sup>C]PyBic in healthy rats.

### Quantitative analysis for rodent PET

IDL programs developed in house in Yale University PET Center was used for rodent and following monkey PET imaging analysis. The simplified reference tissue model 2 (SRTM2) [18] was used to estimate the distribution volume ratio (DVR) using the contralateral as a reference region. The first 60 min dynamic scan data were used in the kinetic modeling analysis, generating similar DVR to using the 90 min dynamic scan data (Supplementary Fig. 3).

## PET imaging in rhesus monkeys

Two rhesus monkeys (*Macaca mulatta*) were used in the study. For Monkey 1, a 120-min long dynamic PET scan (one baseline and one blocking scan with veliparib) was carried out. For Monkey 2, a total of 2 baseline scans (test, retest), 2 blocking scans with veliparib (2.5 mg/kg) and BGB290 (0.5 mg/kg), and one P-gp inhibitor tariquidar (1.4 mg/kg) were carried out on a FOCUS220 scanner.

PET imaging reconstruction was performed using similar procedures as described previously [33]. To define the regions of interest (ROIs), MR images were acquired using a Siemens 3 T Trio scanner and coregistered to an inhouse-generated monkey brain atlas and the PET images. The PET emission data were reconstructed using a Fourier rebinning and filtered back projection algorithm with a Shepp-Logan filter. SUV TACs were generated for the brain stem, cerebellum, frontal cortex, occipital cortex and globus pallidus.

## Ex vivo biodistribution experiments

Seven RG2-bearing rats were used in the ex vivo biodistribution analysis. Briefly, [<sup>11</sup>C]PyBic ( $15.8 \pm 5.0$  MBq) were injected as a bolus in the presence (blocking,  $n = 3$ ) or absence of veliparib (baseline,  $n = 4$ , 5 mg/kg, *i.v.*). Animals were euthanized at 60 min post injection of the radiotracer. Blood and preselected organs, such as the olfactory, cerebellum, brain stem, tumor, muscle, spleen, kidney, liver, lung, and hippocampus, were collected, weighed, and counted in an automatic Wizard  $\gamma$  counter (PerkinElmer). Radioactivity concentrations were normalized against weight, decay-corrected, and expressed as percentage of injected dose per gram tissue (%ID/g) or SUV.

## Western blotting

Western blotting was performed on normal brain and tumor tissues from RG2 rats that were lysed in protein lysis buffer (1% SDS, 10% glycerol, in 25 mM Tris-HCl, pH 6.8) supplemented with proteinase inhibitors (cOmplete™, Cat# 11,836,170,001, Sigma) and phosphatase inhibitors (PhosSTOP™, Cat # 4,906,845,001, Sigma). Three micrograms of protein was separated using WES capillary electrophoresis (ProteinSimple) and incubated with rabbit polyclonal anti-PARP1 antibody (Proteintech, Cat# 13,371-1-AP) in antibody dilution buffer provided with the WES machine. Compass software provided by ProteinSimple was used to analyze the western blot results. The absolute chemiluminescent signal values of the area under the specific peak curve generated by Compass were used to quantify the protein expression level.

## Immunohistochemistry

Sagittal-cut rat brains with RG2 tumors were paraffin-embedded and cut into 10-micron sections and deparaffinized and rehydrated for immunohistochemistry staining of PARP1 using the abovementioned antibody. Slides were blocked with 2% normal goat serum for 1 h, incubated with anti-PARP1 antibody (1:200) overnight at 4 °C, and incubated with biotin-conjugated secondary antibody for 1 h, followed by streptavidin-horseradish peroxidase and substrate application according to the manufacturer's instructions (Vector Labs). Vectashield with DAPI was used for nuclear counterstaining, and sections were scanned using Aperio AT2 at 20× with a minimum of 5 focus points verified prior to automated scanning in Yale Pathology Tissue Services. Images were obtained using Aperio ImageScope (v12.4.3.5008).

## Metabolite analysis

Two different metabolite studies, first with tumor-bearing rats and later with a nonhuman primate, were performed. The activity of the blood sample was measured. The plasma fraction was collected by centrifugation of the blood. For rats, the plasma was mixed with a urea solution and further diluted with a 0.2 mL (80:20) mixture of ammonium formate aqueous solution (0.1 M) and MeCN and run under the same solution as the mobile phase at 1 mL/min in a Gemini HPLC column (NX, 5 $\mu$ ). For NHP plasma metabolite analysis, the NHP plasma was diluted with an HPLC mobile phase comprising an 85:15 ratio of ammonium formate aqueous solution (0.1 M) and MeCN and run in a Gemini NX column at a 1.2 mL/min flow rate.

## Kinetic modeling

Volume of distribution ( $V_T$ , mL·cm<sup>-3</sup>) values were derived through 1-tissue (1 T) compartment, 2TCM, and MA1 kinetic modeling as described before [34]. Nondisplaceable binding potential ( $BP_{ND}$ ) values were calculated from  $V_T$  values based on the formula  $BP_{ND} = (V_T - V_{ND})/V_{ND}$ . Target occupancy and  $V_{ND}$  were calculated using the Lassen plot.

## Statistical analysis

Unpaired and two-sided Student *t* tests were performed using GraphPad Prism. All data are presented as the mean  $\pm$  SD unless described otherwise. In vivo and in vitro experiments were repeated at least 2 times/experiment with the “n” number detailed in the corresponding figure legends. Statistical significance was defined as  $P < 0.05$ .

## Results

### Computational studies

We performed computational studies to analyze the physicochemical properties of PyBic in comparison with veliparib. From the docking study, we found that the secondary interactions of PyBic with PARP1 were consistent with those of veliparib. Then, we calculated the physicochemical and pharmacological parameters, *i.e.*, LogP, MDCK permeability, PSA, LogS, and XP scores, to predict the brain permeability and binding affinity of PyBic (Table 1) [20, 27, 35]. The calculated XP score (-7.866) was slightly higher than that of veliparib (-7.976), which was consistent with their reported  $IC_{50}$  values (6 nM and 5.2 nM for PyBic and veliparib, respectively [36, 37]. With the extra methyl group, PyBic was predicted to possess higher lipophilicity (LogP), lower polar surface area (PSA), and improved membrane permeability (MDCK permeability) than veliparib. Furthermore, we removed a hydrogen bond donor by *N*-methylating pyrrolidine, presumably reducing its liability to P-gp efflux [38]. The changes in physicochemical properties suggested improved BBB penetration for PyBic over veliparib. Therefore, we decided to pursue radiolabeling and *in vitro* and *in vivo* evaluations of PyBic as our lead brain-penetrant PARP PET tracer.

### Chemistry and radiochemistry

We reasoned that [ $^{11}C$ ]PyBic could be obtained via a chemoselective *N*-methylation reaction using [ $^{11}C$ ]MeI and veliparib as the labeling precursor. Veliparib (4) and the PyBic standard (5) were synthesized following the reported procedure with slight modifications (Supplementary Fig. 1a) [39]. The reference standard (5) was synthesized from precursor 4 using either methyl iodide (MeI) under basic conditions in 56% yield or paraformaldehyde in 77% yield.

[ $^{11}C$ ]PyBic was synthesized in  $43 \pm 10\%$  decay-corrected radiochemical yields after formulation (962 to 1554 MBq,  $n=8$ , Supplementary Table 1, Supplementary Fig. 1b). The identity of the purified radiotracer was inferred from the coelution of the radiotracer with PyBic standard compound 5 on radio-HPLC (Supplementary Fig. 1c). Formulated [ $^{11}C$ ]PyBic was obtained with greater than 97% radiochemical purity (RCP) and a molar activity of  $148 \pm 85$  MBq/nmol

( $n=6$ ). The whole production process, starting from the trapping of [ $^{11}C$ ]MeI, including the synthesis, purification and formulation, lasted approximately 60 min.

### LogD measurement

The  $\text{LogD}_{7.4}$  of [ $^{11}C$ ]PyBic was determined to be  $1.76 \pm 0.05$  ( $n=5$ ), which is higher than the calculated LogP value (1.18) but still within the optimal range for BBB penetration [40].

### [ $^{11}C$ ]PyBic PET imaging in RG2-bearing rat brains

To explore the feasibility of using [ $^{11}C$ ]PyBic in rat brain PET imaging, we obtained tritium-labeled PyBic, aka [ $^3H$ ]PyBic (Supplementary Fig. 2a) for saturation binding assays using rat hippocampal homogenates. The  $K_D$  and  $B_{max}$  values in the rat hippocampus were 0.46 nM and 50 fmol/mg (protein), respectively. Assuming the protein content of rat brain tissue is 9.1% and the brain tissue density is 1 g/mL, the calculated  $B_{max}$  was 4.6 nM and the  $B_{max}$  to  $K_D$  ratio was 10, suggesting the feasibility of imaging PARP1 in the rat brain using [ $^{11}C$ ]PyBic (Supplementary Fig. 2b).

To evaluate [ $^{11}C$ ]PyBic in RG2 tumor-bearing rats ( $n=16$ ), we first imaged 12 RG2 tumor-bearing rats for tumor assessment using contrast-enhanced MR (CEMR). The RG2 tumor size ranged from 6.5 to 180.6 mm<sup>3</sup> at 14–18 days post-implantation of tumor cells, and the average size was  $54.6 \pm 56.0$  mm<sup>3</sup> (mean  $\pm$  SD). After confirming tumor formation in the rat brains, we carried out [ $^{11}C$ ]PyBic PET imaging in 9 rats for either a 0–90 min or a 0–60 min scan. The administered dose of [ $^{11}C$ ]PyBic was equivalent to  $0.4 \pm 0.12$   $\mu\text{g}/\text{kg}$  of cold mass of PyBic. In baseline scans ( $n=5$ ), the standardized uptake value (SUV) images summed from 30 to 60 min postinjection (*p.i.*) showed high contrast between the tumor region and the contralateral nontumor brain region, as outlined in Fig. 2a, which was markedly higher than that in the blocking scans ( $n=4$ ), in which veliparib (5 mg/kg, *i.v.*) was administered before tracer injections (Fig. 2b). The tumor uptake plateaued within 30 min *p.i.*, with a baseline tumor SUV of  $1.0 \pm 0.22$  (mean  $\pm$  SD) averaged from 30 to 60 min *p.i.* The contralateral nontumor brain region showed much lower tracer uptake, with an

**Table 1** Binding affinity and physicochemical properties of PyBic and veliparib

	$IC_{50}$	LogP	MDCK	PSA	LogS	XP
PyBic	6 nM	1.18	91.6	77.3	-2.21	-7.866
Veliparib	PARP1: 5.2 nM PARP2: 2.9 nM	0.58	60.57	86.7	-1.693	-7.976
Optimal range [33]	< 10 nM	1–3	25–500	< 90	-6.05–0.5	

average SUV of  $0.39 \pm 0.04$  (mean  $\pm$  SD, Fig. 2c). All the selected normal brain regions showed significantly lower tracer uptake than the tumors ( $p < 0.05$ , Fig. 2c, Supplementary Fig. 3). With the preinjected PARP1/2 inhibitor veliparib (5 mg/kg, *i.v.*), the tumor SUV exceeded 1 within 10 min *p.i.* and then decreased to  $0.39 \pm 0.10$  (mean  $\pm$  SD) after 40 min *p.i.* (Fig. 2d). Veliparib provided 61% blockade of tracer binding based on the SUV (30–60 min) data ( $p = 0.0003$ , *t* test, Fig. 2c-d). Injection of the P-gp inhibitor verapamil ( $n = 1$ ) did not change the brain SUVs compared to baseline injections in healthy rats ( $n = 2$ ) (supplementary Fig. 4), indicating that [ $^{11}\text{C}$ ]PyBic is unlikely a substrate of P-gp. This is consistent with our *in vitro* Caco-2 cell monolayer permeability test results, which showed an efflux ratio of 0.52 for PyBic.

### [ $^{11}\text{C}$ ]PyBic PET quantitative analysis in RG2 rats

For the quantitative PET analysis, we calculated the regional distribution volume ratio (DVR) using the simplified reference tissue method 2 (SRTM2) with the contralateral nontumor region of interest (ROI) defined as shown in Fig. 2a/b as the reference region. The contralateral nontumor ROI was chosen as the reference region because it was the brain region with the lowest tracer uptake and was the least influenced by preinjected veliparib as the blocking drug (Supplementary Fig. 4). Using the pilot 90-min scan data ( $n = 4$ ), we observed a strong linear correlation between DVR (0–60 min) and DVR (0–90 min) (Supplementary Fig. 5). Thus, DVR derived using 0–60 min data is sufficient for [ $^{11}\text{C}$ ]PyBic quantitative analyses, and we used DVRs from 0–60 min scan ( $n = 9$ ) in the following analysis. In the baseline scans, the highest tracer uptake was in the tumor (DVR:  $3.33 \pm 0.40$ ,  $n = 5$ ). The average tumor DVR was decreased by 51% in blocking scans ( $1.62 \pm 0.16$ ,  $n = 4$ ,  $p = 0.049$ , Fig. 2e). There were smaller but statistically significant 28% and 30% differences in DVR between baseline and blocking scans in neocortex and cerebellum, respectively, strongly suggesting that there is PARP-specific uptake in these brain regions. Note that partial volume effects contribute to inter-regional variation in uptake due to differential spill-in from other brain regions and from the extra-cranial tissue. Further confirmation from *ex vivo* and *in vitro* AR study is needed to confirm this *in vivo* imaging finding. Considering the compromised BBB at the tumor site, these data are insufficient to prove the brain penetration of [ $^{11}\text{C}$ ]PyBic, as [ $^{11}\text{C}$ ]PyBic and veliparib might be able to diffuse into healthy brain regions through the leaky BBB around the RG2 tumor. The DVRs of the other brain regions did not show significant differences between baseline and blocking scans, indicating similar PARP1 expression levels in these brain regions and the contralateral cortex.

### [ $^{11}\text{C}$ ]PyBic metabolism study in rats

We examined the radiometabolites in rat plasma and brain ( $n = 4$ ) at 60 min *p.i.* of [ $^{11}\text{C}$ ]PyBic. The parent fraction of [ $^{11}\text{C}$ ]PyBic at 60 min *p.i.* was 31% and 90% in the plasma and brain, respectively. We detected two major radiometabolite peaks with HPLC retention times of approximately 3.5 min and 6.5 min, while the retention time of the parent tracer was approximately 5 min (Fig. 2f).

### Ex vivo biodistribution study

To validate the PET imaging results and determine the extent of nonspecific binding, biodistribution studies of [ $^{11}\text{C}$ ]PyBic in RG2 rats were performed at 60 min *p.i.* with (blocking,  $n = 3$ ) or without preinjected veliparib (baseline,  $n = 4$ ). We expect to see complete PARP1/2 blockade at the *i.v.* dose of 5 mg/kg, as the estimated  $C_{\max, \text{plasma}}$  (1.64  $\mu\text{M}$ ) is 328-fold of the  $IC_{50}$  of veliparib and the estimated  $C_{\max, \text{brain}}$  (0.42  $\mu\text{M}$ ) is 84-fold of the  $IC_{50}$  of veliparib [41]. The biodistribution data showed that [ $^{11}\text{C}$ ]PyBic had the highest uptake in the tumor ( $0.85 \pm 0.3\% \text{ID/g}$ ,  $n = 4$ ) and spleen ( $2.85 \pm 0.3\% \text{ID/g}$ ,  $n = 4$ ). The uptake of [ $^{11}\text{C}$ ]PyBic was reduced by 75% ( $n = 4$ ,  $p = 0.021$ ) and 74% ( $n = 4$ ,  $p = 0.0004$ ) in the tumor and spleen, respectively, by veliparib preadministration (Fig. 3a). The mean tumor uptake as represented by SUV ( $1.97 \pm 0.68$ ,  $n = 4$ ) derived from the biodistribution data was nearly twice the mean tumor PET SUV (Supplemental Fig. 6). The difference between PET and biodistribution data is likely due to partial volume effects associated with small animal PET imaging. Interestingly, the tissue-to-plasma ratios for [ $^{11}\text{C}$ ]PyBic at 60 min *p.i.* under the blocking condition are comparable to those of [ $^3\text{H}$ ]veliparib under similar blocking conditions (veliparib, 5 mg/kg, *i.v.*) for the spleen, kidney, liver, and lung, indicating similar levels of nonspecific binding for these two tracers in these selected tissues. However, [ $^{11}\text{C}$ ]PyBic exhibits a lower nonspecific signal in muscle and relatively higher nonspecific signals in the brain than [ $^3\text{H}$ ]veliparib (Supplemental Table 2) [42]. The mean tissue-to-plasma ratios for [ $^{11}\text{C}$ ]PyBic in selected rat tissues were as follows: brain (0.9), kidney (5.3), liver (4.7), lungs (2.4), spleen (4.0), muscle (2.2) at 60 min *p.i.* under blocking conditions with preinjected veliparib (5 mg/kg, *i.v.*).

Using data from the biodistribution study, we compared the tracer uptake in tumors normalized by different brain regions, muscle, and blood and found that tumor-to-blood ratios showed the greatest difference between baseline and blocking groups ( $8.39 \pm 2.10$ ,  $n = 4$ ;  $1.05 \pm 0.29$ ,  $n = 3$ , for baseline and blocking groups, respectively,  $p = 0.032$ , Fig. 3b), indicating ubiquitous baseline PARP expression in rodent brain and muscle. Compared with using other brain regions as the reference region, the tumor-to-contralateral cortex (tumor/cortex) ratios of the



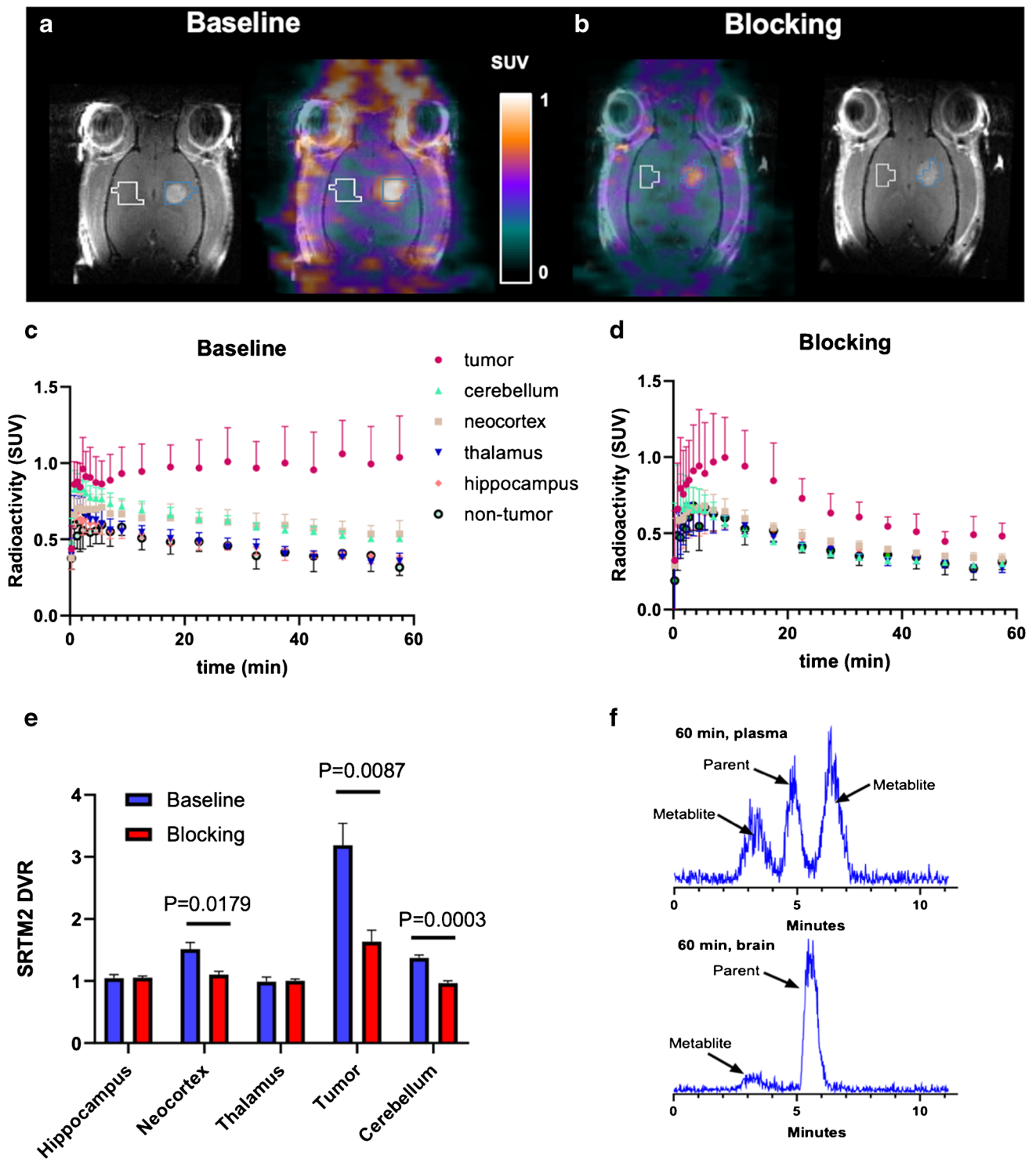


**Fig. 2** [<sup>11</sup>C]PyBic PET imaging in RG2 glioblastoma-bearing rats and quantitative data analysis results. Representative horizontal summed PET standard uptake value (SUV) images from 30–60 min p.i. and the corresponding contrast-enhanced MR (CEMR) images for baseline (a) and blocking scans (b), with hand-drawn regions of interest (ROIs) for tumor and contralateral nontumor regions. (c–d) SUV time-activity curves (TACs) of the RG2 tumor and selected brain subregions, including the contralateral nontumor cortex (nontumor), neocortex, thalamus, hippocampus, brain stem, and cerebellum, under

baseline (c, n=5) and blocking (d, n=4) conditions. (e) The regional distribution volume ratios (DVRs) of [<sup>11</sup>C]PyBic in selected brain subregions and tumors, calculated using the simplified reference tissue method 2 (SRTM2) with the contralateral nontumor region as the pseudo reference region. The DVRs of the tumor (p=0.0087), cerebellum (p=0.0003), and neocortex (p=0.0179) showed statistically significant differences between baseline and blocking scans. (f) Radiometabolite analysis of [<sup>11</sup>C]PyBic in rat plasma and brain homogenate at 60 min p.i.

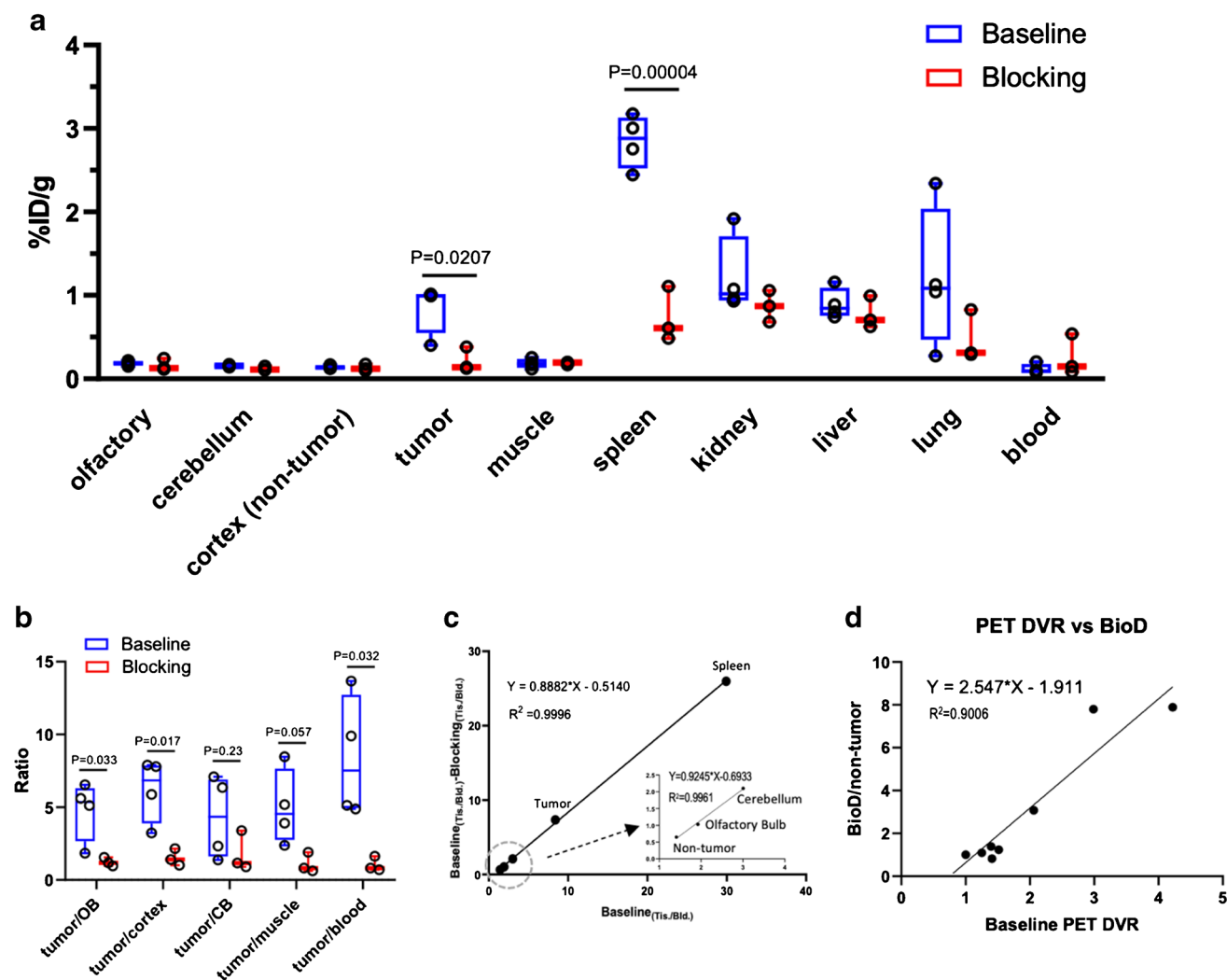


**Fig. 3** (a) Biodistribution analysis of baseline and blocking (veliparib, 5 mg/kg) at 60 min p.i. of [ $^{11}\text{C}$ ]PyBic, expressed as %ID/g ( $n=4$  for baseline;  $n=3$  for blocking), with tumor and spleen showing statistically significant differences at baseline and blocking studies. (b) The ratio of tracer uptake in tumor to different tissues and blood, showing that the tumor-to-contralateral cortex (tumor/cortex) ratios at baseline study and blocking study are most significantly different ( $p=0.017$ ), supporting the use of contralateral nontumor region as the reference region in the SRTM2 analysis. (c) Linear correlational analysis of the difference between the tissue-to-blood ratios at baseline and blocking

studies and baseline tissue-to-blood ratios. Dots on the graph represent the mean values of each analyzed brain region or tissue, i.e., the olfactory bulb, cerebellum, tumor, contralateral nontumor cortex (nontumor), and spleen. (d) Linear correlational analysis of the results of baseline SRTM2 DVR and biodistribution data on tracer uptake in the cerebellum, nontumor, tumor, and brain stem, normalized by nontumor tracer uptake. Dots on the graph represent each individual tissue of cerebellum, tumor, contralateral nontumor cortex (nontumor), and brain stem from three different rats. For the statistical analysis using a  $t$  test,  $p < 0.05$  was considered significantly different

baseline and blocking groups had the greatest statistical significance ( $6.2 \pm 2.1$ ;  $1.5 \pm 0.6$ , for baseline and blocking studies, respectively,  $p = 0.017$ , Fig. 3b), supporting the use of the contralateral nontumor cortex region as the reference region in the PET data analysis. We also plotted the difference in tissue-to-blood ratios between baseline and blocking studies against the tissue-to-blood ratios at baseline for the spleen, tumor, olfactory bulb, cerebellum, and neocortex, which showed excellent linearity and fit ( $Y = 0.89 * X - 0.51$ ,  $R^2 = 0.9996$ , Fig. 3c),

indicating high PARP-specific tracer uptake in these tissues [43–45]. The baseline PET DVR values of the tumor, contralateral nontumor cortex, hippocampus, brain stem and cerebellum correlated well with the biodistribution data ( $Y = 2.547 * X - 1.911$ ,  $R^2 = 0.9$ , Fig. 3d), which supported the use of SRTM2 for the quantitative analysis of PET imaging data in RG2 rats. PET DVR values were lower than the biodistribution data, indicating underestimation of the ratios in the PET results, likely due to partial volume effects in the tumor.

**Table 2** Volume of distribution ( $V_T$ ) values ( $\text{mL}/\text{cm}^3$ ) of [ $^{11}\text{C}$ ]PyBic in two nonhuman primates (NHPs) under baseline conditions or with preinjected Veliparib, BGB290, or tariquidar

Brain region	Monkey 1		Monkey 2				P-gp inhibition
	Baseline	Blocking	Baseline		Blocking		
		Veliparib	Test	Retest	Veliparib	BGB290	
brainstem	11.0	2.1	8.4	9.1	1.6	1.5	8.0
caudate	10.8	2.4	14.7	9.4	2.2	2.4	8.4
cerebellum	17.6	2.3	14.9	14.0	2.0	1.8	12.4
cingulate	11.9	2.6	14.6	14.0	2.9	3.2	12.4
frontal cortex	12.9	2.4	19.7	18.2	2.8	3.0	14.6
insula	12.3	2.6	11.2	12.7	2.4	2.9	10.9
occipital cortex	15.5	2.2	16.3	15.8	2.0	2.2	13.5
pons	11.6	2.2	8.0	9.9	1.6	1.6	8.9
putamen	13.8	2.5	9.5	11.9	2.1	2.4	10.4
temporal cortex	12.9	2.3	14.7	13.8	2.3	2.6	12.0
thalamus	11.2	2.4	6.9	7.7	1.8	2.2	7.8

### PARP1 expression correlates with in vivo [ $^{11}\text{C}$ ]PyBic uptake

Immunohistochemical (IHC) staining of PARP1 in RG2-bearing rat brains indicated that PARP1 expression in tumor tissues was noticeably higher than that in normal brain tissue (Fig. 4a). The expression of PARP1 was heterogeneous across the tumor tissues, with the tumor border exhibiting the highest PARP1 expression (Fig. 4b). Using capillary electrophoresis western blotting (WES), we compared the expression of PARP1 in the cortex, olfactory bulb, brain stem, cerebellum, hippocampus, and tumor. Consistent with the in vivo PET imaging, ex vivo biodistribution, and in vitro IHC results, tumor tissues expressed significantly higher levels of PARP1 compared to the cortex ( $p=0.0036$ ), brain stem ( $p=0.0041$ ), and hippocampus ( $p=0.0013$ ) (Fig. 4c–d, Supplementary Fig. 7), with the lowest levels found in the brain stem and hippocampus. We further carried out linear correlational analyses between WES, biodistribution and PET imaging and found a positive linear correlation between WES and biodistribution data ( $Y=406,275 \cdot X+118,898$ ,  $R^2=0.88$ , Fig. 4e), as well as between WES and PET data ( $Y=143,581 \cdot X-13,574$ ,  $R^2=0.84$ , Fig. 4f).

### In vivo NHP PET imaging study with [ $^{11}\text{C}$ ]PyBic

To facilitate clinical translation and confirm the brain penetration of [ $^{11}\text{C}$ ]PyBic in larger animals with intact BBB, we performed PET imaging studies in healthy NHPs, with the collection of arterial blood for metabolism analysis and generation of arterial input function (AIF). [ $^{11}\text{C}$ ]PyBic (194 MBq, mean,  $n=2$ ) was injected into one healthy rhesus monkey (Monkey 1) with or without veliparib (2.5 mg/kg, *i.v.* and scanned for 2 h. A second monkey (Monkey

2) was injected with [ $^{11}\text{C}$ ]PyBic (256 MBq  $\pm$  83 MBq,  $n=5$ ) and scanned twice under baseline conditions for a test–retest comparison, once with preinjected veliparib (2.5 mg/kg, *i.v.*), once with preinjected BGB290 (PARPi, 0.5 mg/kg, *i.v.*), and once with the infusion of the P-gp inhibitor tariquidar (1 mg/kg, *i.v.* over 30 min) to study the effect of P-gp inhibition on the brain uptake of [ $^{11}\text{C}$ ]PyBic. Summed baseline SUV images from the early time (10–20 min *p.i.*) and late time windows (60–90 min *p.i.*) showed fast tracer entrance into the brain and sustained retention in all brain regions (Fig. 5a), consistent with the ubiquitous expression pattern of PARP1 in the monkey brain [46]. The test and retest studies in the same animal showed nearly perfect overlap of the AIF (Supplementary Fig. 8a). In the blocking scan, the early SUV (10–20 min) was higher than the baseline SUV, which was due to the increased tracer plasma concentration caused by the blockade of peripheral PARP1/2 binding by veliparib (Supplementary Fig. 8b). Similarly, BGB290, a structurally different PARP1/2 inhibitor, also increased plasma and brain SUVs in the earlier period compared to baseline (Supplementary Fig. 8c). Injection of the P-gp inhibitor tariquidar did not change the AIF compared to the baseline study (Supplementary Fig. 8d). The late-time SUV (60–90 min) images of the blocking scans showed consistently low and nearly homogeneous tracer distribution in all brain regions, indicating effective blockade by veliparib and BGB290 at the injected doses. From the baseline time-activity curves (TACs), the cerebellum had the highest uptake, followed by the occipital cortex, frontal cortex and globus pallidus, showing the lowest tracer uptake, while in the blocking scans, the tracer washed out of the brain quickly, with reduced contrast among brain regions at later imaging windows due to the effective blockade of PARP binding sites in all brain regions (Fig. 5b–c).

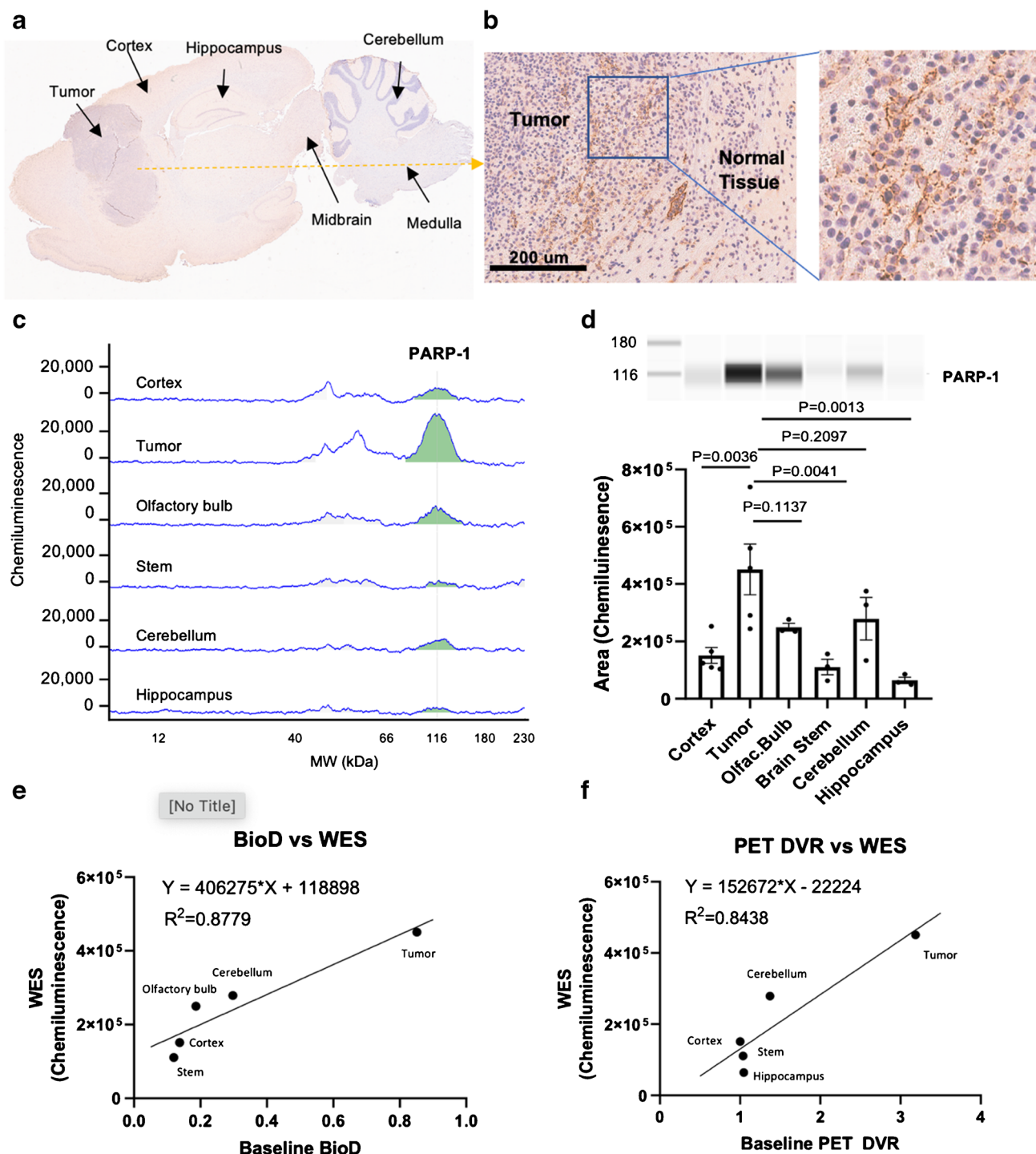


**Fig. 4** Immunohistochemical (IHC) staining and western blotting of PARP1 and correlation analysis with biodistribution and PET results. **(a)** Representative IHC staining of PARP1 in RG2 tumor-bearing rats. **(b)** PARP1 IHC in tumor tissue and adjacent normal tissue. **(c-d)** Representative western blotting of PARP1 in selected brain subregions, including the cortex, olfactory bulb, brain stem, cerebellum, hippocampus, and tumor, using a capillary electrophoresis WES system (ProteinSimple). **(e)** Histogram graph of PARP1 expression. The

116 kD band was detected by the PARP1-specific antibody. **(d)** Classic western blotting image of PARP1 and expression quantification.  $N=3-4$ , multiple t test,  $p < 0.05$  is considered significantly different. **(e)** Correlation of baseline biodistribution and WES on the olfactory bulb, stem, cerebellum, hippocampus, and tumor. **(f)** Correlation of baseline PET DVR and PARP1 WES in the tumor, cerebellum, cortex, brain stem, and hippocampus. For graphs **e** and **f**, dots on the graph represent the group mean, with  $n = 3-5$  per group

## [<sup>11</sup>C]PyBic metabolism study in NHP

Similar to the rat metabolism study, we observed the same two major radiometabolite peaks from the radio-HPLC chromatograms, indicating cross-species conservation in the metabolism profiles of [<sup>11</sup>C]PyBic. The metabolism rate of this tracer was moderate in NHPs, with plasma parent fractions of 73% and 52% at 15 min and 90 min *p.i.*, respectively (Fig. 5d). We do not expect the radiometabolites to be brain penetrant, at least not to an extent enough to interfere with the quantification of PARP1 in the brain, based on the rat brain homogenate radio-HPLC data (Fig. 2f).

## Brain PET kinetic modeling in NHPs

To estimate the regional distribution volume ( $V_T$ ) and the ratio of tracer concentration in the brain to that in plasma at equilibrium, we compared the use of the 1-tissue compartment model (1TCM), 2-tissue compartment model (2TCM) and multilinear analysis (MA1) method. Both the 1TCM and MA1 methods produced good fits with the TACs, with 1TCM producing more reliable brain regional  $V_T$  values, which are consistent with the MA1  $V_T$  values (supplementary Fig. 9), while the 2TCM produced  $V_T$  with large standard errors in several brain regions. We thus used  $V_T$  from 1TCM in the following analysis. Based on the Lassen plot analysis, both the structurally analogous veliparib and the structurally dissimilar PARPi BGB290 blocked more than 90% of the binding of [<sup>11</sup>C]PyBic in the monkey brains (Fig. 6), indicating the high *in vivo* binding specificity of [<sup>11</sup>C]PyBic. The mean nondisplaceable volume of distribution ( $V_{ND}$ ) of [<sup>11</sup>C]PyBic was 1.81 mL/cm<sup>3</sup>. The  $V_T$  values from 1TCM in the monkey baseline scan ranged from 7.3 mL/cm<sup>3</sup> for the amygdala to 15.5 mL/cm<sup>3</sup> for the occipital cortex (Table 2), while the  $V_T$  values for the monkey blocking scan ranged from 2.1 mL/cm<sup>3</sup> to 2.7 mL/cm<sup>3</sup>. Both  $K_1$  and  $V_T$  calculated using 1 T models were similar between the test and retest baseline as well as with the P-gp inhibition scan using tariquidar as the P-gp inhibitor (Supplementary Table 3).

Using the average  $V_{ND}$  from three blocking scans, we obtained the nondisplaceable binding potential ( $BP_{ND}$ ) (Supplementary Table 4) for the brain regions of the two monkeys. We found that the brainstem had the lowest  $BP_{ND}$ , while the frontal cortex and occipital cortex had relatively higher  $BP_{ND}$ .

## Discussion

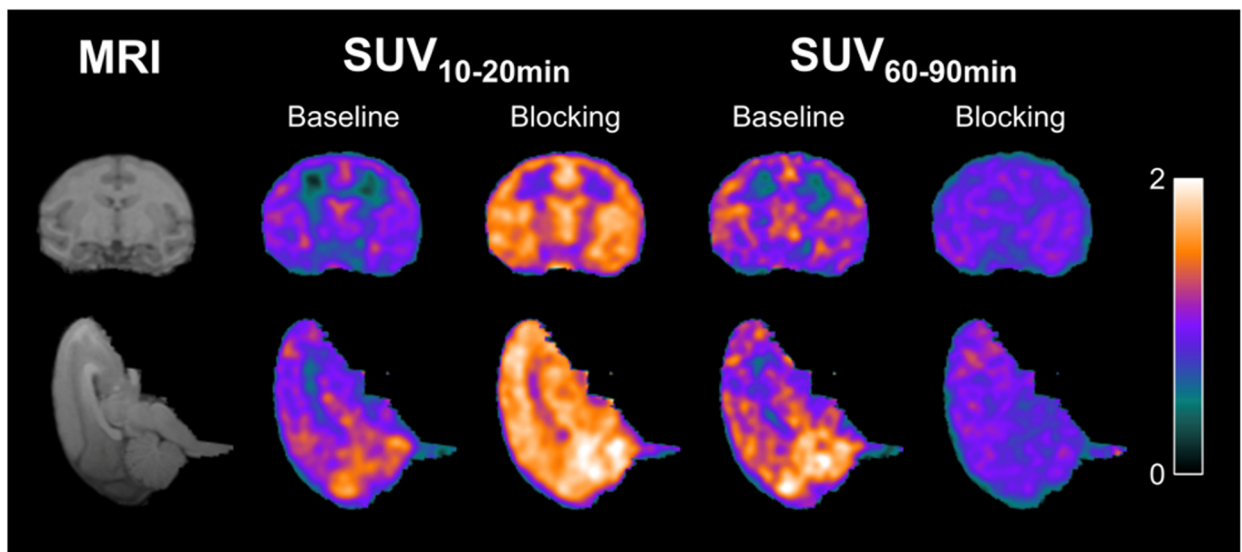
In this study, we developed and evaluated a novel brain-penetrant PARP radiotracer, [<sup>11</sup>C]PyBic, for PET imaging and *in vivo* quantification of PARP in the healthy brain and RG2

rat glioblastoma model. PET imaging results showed higher tracer uptake in the orthotopic RG2 glioblastoma relative to the rest of the rat brain. The quantification of PARP1 using molecular biological methods and biodistribution analysis confirmed the PET imaging results. The uptake of [<sup>11</sup>C]PyBic is significantly reduced by the PARP1/2 inhibitor veliparib in both PET imaging and biodistribution analysis, indicating the *in vivo* binding specificity of the radiotracer. The high brain-to-plasma ratio in healthy NHPs demonstrated the high brain permeability and specific binding of [<sup>11</sup>C]PyBic in NHPs, supporting its use as a brain PARP PET imaging probe.

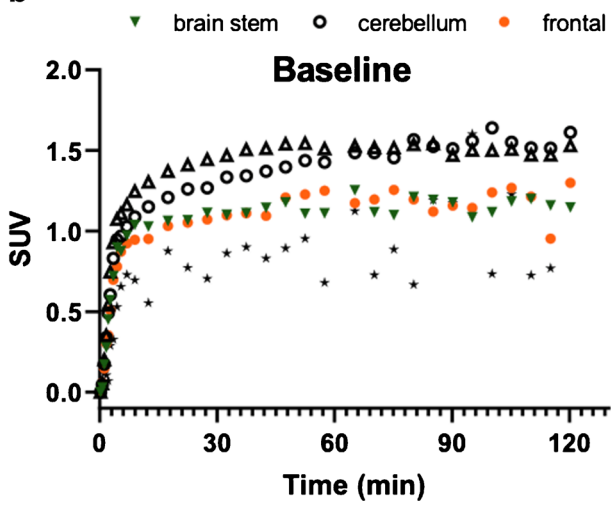
Several PARPi-derived PET radiotracers have been developed for PARP imaging. Tu et al. reported the first PET tracer [<sup>11</sup>C]PJ34 intended for imaging PARP in a streptozotocin-induced type I diabetes-related necrosis model, where they found a higher uptake of [<sup>11</sup>C]PJ34 in both the pancreas and liver [47]. Two <sup>18</sup>F-labeled analogs of olaparib, [<sup>18</sup>F]FBO and [<sup>18</sup>F]PARP-FI, have been used to image rodent models of ovarian cancer, pancreatic cancer, and glioma [48, 49]. PET studies on the rucaparib/AG14699-derivative [<sup>18</sup>F]FluorThanatrace ([<sup>18</sup>F]FTT) demonstrated high tracer uptake in a xenograft model of human breast cancer [50]. The first clinical PARP PET imaging study using [<sup>18</sup>F]FTT in ovarian cancer patients (NCT02469129) indicated a positive correlation between tumor SUVs and PARP1 expression levels [51]. In addition, a study using [<sup>18</sup>F]FTT showed the highest tracer uptake in the spleen, pancreas, and liver in healthy human volunteers and the tumor regions of pancreatic ductal adenocarcinoma, biphenotypic hepatocellular carcinoma and cholangiocarcinoma among the 8 different malignant tumors examined [51]. Recently, Carney et al. explored the drug engagement of different PARPis in small-cell lung cancer patient-derived xenografts (PDX) using [<sup>18</sup>F]PARPi and the fluorescent probe PARPi-FL, which have important implications in PARPi drug development, treatment planning and monitoring in the clinic [52]. [<sup>18</sup>F]PARPi has been evaluated in GBM patients recently, but its brain imaging characteristics have not yet been studied in healthy animals or humans [19]. Adam et al. reported a PET imaging probe ([<sup>18</sup>F]SuPAR), a radiofluorinated NAD<sup>+</sup> analog that can be recognized by PARP and incorporated into the long-branched PAR for measuring PARP activity. With [<sup>18</sup>F]SuPAR, they were able to map the dose- and time-dependent activation of PARP following radio/chemotherapy in breast and cervical cancer xenograft models [53]. Zhou et al. reported the radiosynthesis of [<sup>18</sup>F]talazoparib, and the preliminary biodistribution studies in the murine PC-3 tumor model showed that [<sup>18</sup>F]talazoparib had a good level of tumor uptake that persisted for over 8 h [54].

Both olaparib and rucaparib have relatively high PARP trapping capability, which makes them good candidates as cancer therapeutics. However, neither of them nor their

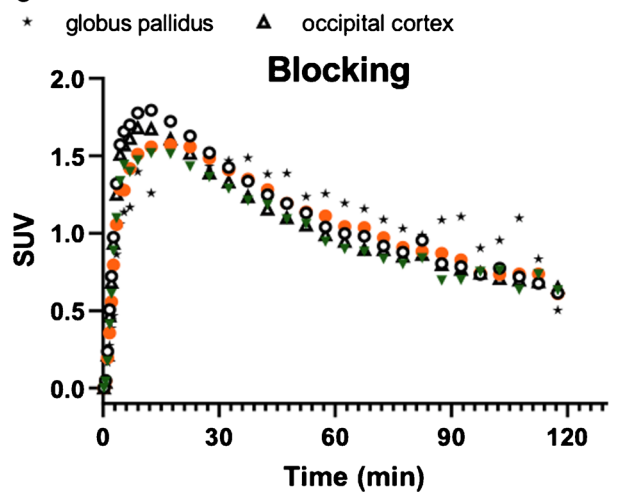
**a**



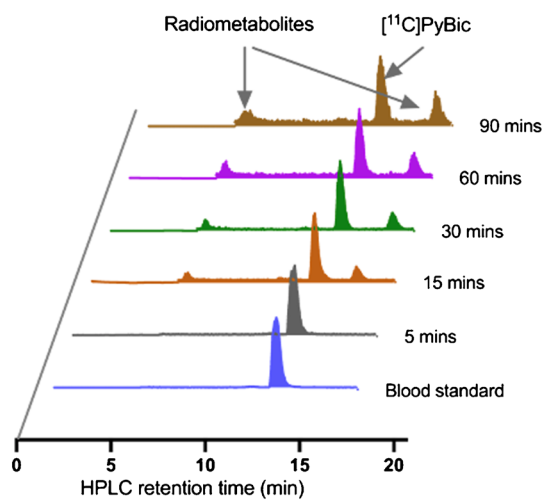
**b**



**c**



**d**



**e**

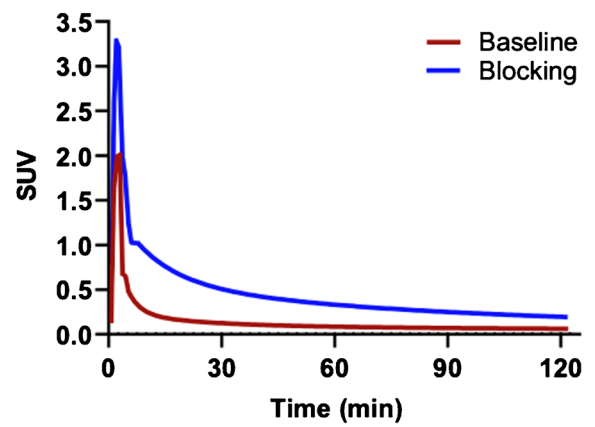


**Fig. 5** [ $^{11}\text{C}$ ]PyBic PET imaging and metabolism study in Monkey 1. (a) MRI of monkey brain (left column) and summed SUV PET images of [ $^{11}\text{C}$ ]PyBic from early (2<sup>nd</sup> and 3<sup>rd</sup> columns, 10–20 min) and late (4<sup>th</sup> and 5<sup>th</sup> columns, 60–90 min) scan windows. The brain regional SUVs ranged from 0.5 to 1.5, with cerebellum being the highest, followed by occipital cortex, frontal cortex and globus pallidus showing the lowest tracer uptake. (b–c) Representative time active curves (TACs) of different brain regions at baseline scan (b) and blocking scan (c). (d) Radio-HPLC chromatograms of plasma samples taken at different time points and the blood standard. (e) Metabolism-corrected arterial blood input functions of a baseline scan (in maroon) and a blocking scan (in blue) in the same monkey

analogs have been shown to achieve desirable brain penetration as PET imaging agents due to their liability to active drug efflux [25, 26]. Compared to olaparib and rucaparib, veliparib (ABT-888) has a relatively lower PARP trapping capability [55] and is reported to be a weak P-gp substrate, which makes it appealing as a lead compound for developing brain PET imaging agents with fast and reversible brain kinetics. Encouraged by our *in silico* prediction results, we synthesized an *N*-methylated derivative of veliparib, PyBic, on the premise that the removal of the N–H hydrogen-bond donor would further decrease its susceptibility to active efflux at the BBB [38] and that the slightly increased hydrophobicity would improve its cell membrane permeability and BBB penetration.

We tested the imaging characteristics of [ $^{11}\text{C}$ ]PyBic in a syngeneic rat model of glioblastoma. PARP1 is constitutively expressed in most tissue types, and it has been found to be upregulated in many different malignant cells, including brain tumors [56]. To test the *in vivo* binding specificity of this tracer and explore its brain penetration at the same time, we chose the syngeneic RG2 rat model, where RG2 glioblastoma cells were orthotopically injected into the right striatum of Fischer 344 (F344) rats, as the chemotherapeutic refractory RG2 rat brain tumor model has been used in the evaluation of PARP1's therapeutic effects [57].

Due to the difficulties in obtaining arterial blood for arterial input function generation in rats, we opted to use the simplified reference tissue method 2 (SRTM2) for quantitative imaging analysis. Except for tumors, all brain regions showed similarly low tracer uptake, reflecting a relatively low level of PARP1 expression in normal rat brain tissue. As shown in supplementary Fig. 4, there was no significant difference in the contralateral nontumor cortex SUV between baseline and blocking scans, while in both the cerebellum and neocortex, the blocking effect was more prominent. We thus chose the contralateral nontumoral cortex as the reference region to estimate the regional DVR [58, 59]. In addition to RG2 tumors, only the cerebellum and neocortex showed significant blocking effects based on the DVR results (Fig. 2e,  $p = 0.0003$ , 0.0179, for cerebellum and neocortex, respectively). Importantly, our biodistribution results correlated well

with the PET DVR, corroborating the SRTM2 analysis results. Our western blotting and immunohistochemical staining results indicate that PARP1 expression at the tumor site is higher than that in normal brain tissue, which is consistent with the biodistribution and PET imaging results.

We calculated the tissue-to-blood ratios using the biodistribution data at 60 min *p.i.* and plotted the difference in the baseline and blocking tissue-to-blood activity ratios against the baseline tissue-to-blood ratios to estimate the PARP occupancy by the pre-administered veliparib. We obtained a nearly perfect linear correlation with an R square of 0.9996 and a slope of 0.89, indicating that approximately 89% PARP is occupied by the pre-administered veliparib at 5 mg/kg (Fig. 3c). This finding indicates highly PARP-specific uptake of [ $^{11}\text{C}$ ]PyBic in RG2 tumors, rat brains and spleens.

Our gadolinium contrast-enhanced MR (CEMR) imaging indicated that the BBB surrounding the RG2 tumors was compromised (Fig. 2). Thus, the PARP-specific uptake of [ $^{11}\text{C}$ ]PyBic in the RG2 rat brains does not exclude the possibility that the tracer is entering the brain through the damaged BBB and/or the BTB around the tumors. Caution should be taken when interpreting the kinetics modeling results. To confirm and quantify the extent of brain penetration of [ $^{11}\text{C}$ ]PyBic, we imaged two healthy NHPs after intravenous bolus injections of [ $^{11}\text{C}$ ]PyBic. To our satisfaction, we observed quick uptake of [ $^{11}\text{C}$ ]PyBic in the NHP brain, plateauing within 30 min *p.i.*, with baseline SUVs ranging from 0.66 (in the globus pallidus) to 0.97 (in the cerebellum) (Fig. 5a–b). Furthermore, we performed blocking scans with preinjected veliparib or BGB290, both of which decreased tracer uptake to nonspecific levels in the whole brain, indicating that [ $^{11}\text{C}$ ]PyBic uptake in monkey brains is indeed PARP-specific. We noticed that the brain kinetics of [ $^{11}\text{C}$ ]PyBic is slower in NHP than in rats. Yet, the NHP brain TACs fit well with 1TC model, suggesting reversible *in vivo* binding of [ $^{11}\text{C}$ ]PyBic in the NHP brain. The faster clearance in the rodent brain is most likely due to faster plasma clearance, as suggested by the lower parent fraction data in the rodent. This is a common difference between rodent and NHP data, *i.e.*, that metabolism is faster in the rodent, so plasma clearance and brain clearance is more pronounced.

We collected arterial blood samples and analyzed the metabolism profiles of [ $^{11}\text{C}$ ]PyBic in rats and NHPs and found two major metabolite peaks of [ $^{11}\text{C}$ ]PyBic in both species (Fig. 2f, 5d). Based on the metabolism profile of veliparib [60–62], we speculated that the oxidation product (compound 6) of methylpyrrolidine is the major radiometabolite. Based on the effective blocking by veliparib in the rodent and NHP PET imaging and the fact that we only detected a minimum amount of radiometabolites in the rat brain homogenates (Fig. 2f), we do not expect the

**Fig. 6** In vivo target occupancy assays shown by Lassen plots of  $V_T$  derived from 1 tissue compartment (1TC) modeling in two different monkeys. **(a)** Lassen plot of  $V_T$  (baseline) vs the difference in  $V_T$  (baseline) and  $V_T$  (blocking) with veliparib as a blocking drug in Monkey 1. **(b)** Lassen plot of  $V_T$  (baseline) vs the difference in  $V_T$  (baseline) and  $V_T$  (blocking) with veliparib as a blocking drug in Monkey 2. **(c)** Lassen plot of  $V_T$  (baseline) vs the difference in  $V_T$  (baseline) and  $V_T$  (blocking) with BGB290 as a blocking drug in Monkey 2. The x-intercept is the estimated nondisplaceable volume distribution (VND), and the slope is the target occupancy

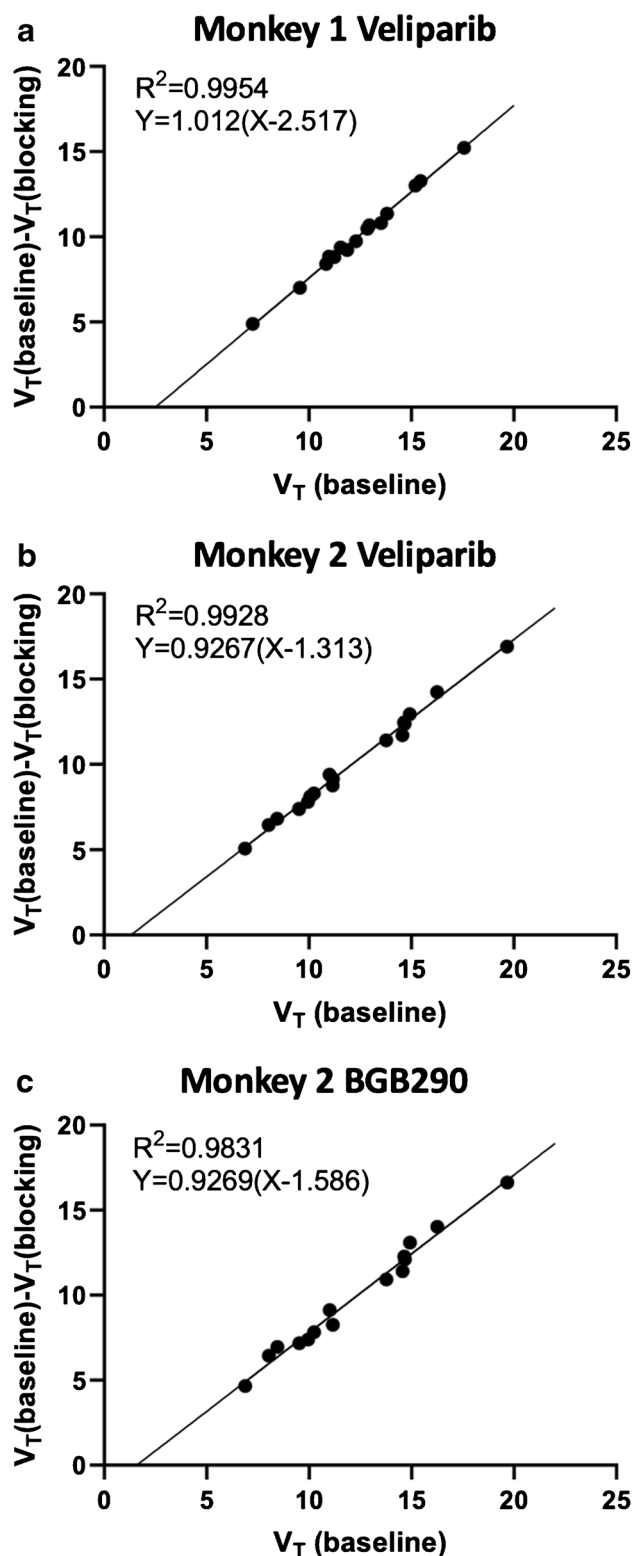
radiometabolites to interfere with the interpretation of the brain PET imaging results.

Compared to other PARP1/2 inhibitors, such as olaparib, talazoparib, and rucaparib, veliparib has a lower PARP trapping capability, implicating a faster  $K_{off}$  rate than other PARP1/2 inhibitors, a desirable feature for quantitative brain PET imaging. Although [ $^{18}F$ ]PARPi has been used in GBM patients to delineate tumors [63], a highly brain-penetrant PET tracer such as [ $^{11}C$ ]PyBic is desirable for reliable PARP quantification and is potentially applicable in lower grade gliomas and brain metastases with intact or heterogeneous BBB integrity.

Because the other PARP PET tracers under development suffer from being P-gp substrates, we examined the effect of P-gp inhibition on the brain uptake and kinetics of [ $^{11}C$ ]PyBic in rats and NHPs. The veliparib can block the brain uptake of PyBic effectively at the doses of 5 mg/kg in rats and 2.5 mg/kg in monkeys, because sufficient amount of veliparib can reach its target in the brain, even though it is a weak substrate of p-gp. This is consistent with previous results using veliparib at 3.1 mg/kg/d to 25 mg/kg/d, which increased the efficacy of temozolomide in rat glioma model [64]. The efflux ratio of veliparib in MDR1-MDCK cells was 1.8, indicating veliparib as a weak P-gp substrate. We measured the efflux ratio of PyBic to be 0.52, indicating PyBic is not a P-gp substrate. Generally, compounds with efflux ratio greater than 2 are considered to be positive P-gp substrates. Our preliminary PET imaging experiment using the P-gp inhibitor verapamil (1 mg/kg, i.v., 10 min before radiotracer injection) did not show obviously altered [ $^{11}C$ ]PyBic uptake in healthy rat brains (Supplementary Fig. 5), indicating that [ $^{11}C$ ]PyBic is unlikely a P-gp substrate. Consistently, our preliminary P-gp inhibition study in NHP showed no influence of the P-gp inhibitor tariquidar on the  $V_T$  and  $K_1$  of [ $^{11}C$ ]PyBic in NHP brain (Supplementary Table 3).

## Conclusions

In summary, we developed and evaluated the first brain-penetrant PARP PET tracer, [ $^{11}C$ ]PyBic, using the RG2 rat glioma model and healthy nonhuman primates for PARP PET imaging. This PET imaging method is expected to



help stratify patients with differential PARP expression and select those who are most likely to benefit from PARPi treatment, thus impacting effective cancer treatment. Furthermore, because PARP1 is associated with the pathogenesis



of Alzheimer's disease (AD), Parkinson's disease (PD), and other central nervous system (CNS) diseases [65, 66], it is expected to have a broader impact in the investigations of PARP status in these CNS diseases, which, hopefully, could lead to an improved understanding of these diseases and open novel therapeutic avenues.

**Supplementary Information** The online version contains supplementary material available at <https://doi.org/10.1007/s00259-023-06162-y>.

**Acknowledgements** The authors appreciate the staff at the Yale PET Center for their technical assistance and would like to thank Andrew Gifford, Sarah J. Routledge, and Kiran Shabir for their technical support in the binding assays.

**Author contribution** D.O., R.P., J.T., J.R., Y.H., Z.C. contributed to the design and synthesis of the radioligand. B.C., T.T., M.L., M.T., D.H., K.F., H.D.F., R.E.C. contributed to the animal imaging and ex vivo and in vitro validation studies. M.K., L.Z., and M.Q.Z. performed the metabolism analysis. H.D.F. acquired MRI data and analyzed tumor volumes. R.E.C. and Y.H. supervised the PET imaging study. B.C., D.O., Z.C. drafted the article. Z.C. conceived and supervised the whole study. All authors contributed to the final version of the manuscript.

**Funding** This study is supported by the National Cancer Institute of the National Institutes of Health under Award Number R03CA249569. This publication was made possible by CTSA grant UL1 RR024139 from the National Center for Advancing Translational Sciences (NCATS), a component of the National Institutes of Health (NIH). The content is solely the responsibility of the authors and does not necessarily represent the official views of the National Institutes of Health.

**Data availability** Imaging data are available upon reasonable request to the corresponding author.

## Declarations

**Ethical approval** PET imaging experiments were performed in rats and rhesus monkeys (*Macaca mulatta*) according to the protocols approved by the Yale University Institutional Animal Care and Use Committee. All applicable international, national, and institutional guidelines for the care and use of animals were followed.

**Conflicts of interest** The authors declare no conflicts of interest related to this work.

## References


- Lord CJ, Ashworth A. PARP inhibitors: Synthetic lethality in the clinic. *Science*. 2017;355:1152–8.
- Alavi A, Lakhani P, Mavi A, Kung JW, Zhuang H. *Radiol Clin North Am*. 2004;42:983.
- Chiarugi A, Moskowitz MA. PARP-1—a perpetrator of apoptotic cell death? *Science*. 2002;297:200–1.
- Delgado-Lopez PD, Corrales-Garcia EM. Survival in glioblastoma: a review on the impact of treatment modalities. *Clin Transl Oncol*. 2016;18:1062–71.
- Arvanitis CD, Ferraro GB, Jain RK. The blood–brain barrier and blood–tumour barrier in brain tumours and metastases. *Nat Rev Cancer*. 2020;20:26–41.
- Petterson SA, Sørensen MD, Kristensen BW. Expression profiling of primary and recurrent glioblastomas reveals a reduced level of pentraxin 3 in recurrent glioblastomas. *J Neuropathol Exp Neurol*. 2020;79:975–85.
- Arvanitis CD, Ferraro GB, Jain RK. The blood–brain barrier and blood–tumour barrier in brain tumours and metastases. *Nat Rev Cancer*. 2020;20:26–41.
- Sarkaria JN, et al. Is the blood–brain barrier really disrupted in all glioblastomas? A critical assessment of existing clinical data. *Neuro Oncol*. 2018;20:184–91.
- Murnyak B, et al. PARP1 expression and its correlation with survival is tumour molecular subtype dependent in glioblastoma. *Oncotarget*. 2017;8:46348–62.
- Schaller BJ, Modo M, Buchfelder M. Molecular imaging of brain tumors: a bridge between clinical and molecular medicine? *Mol Imaging Biol*. 2007;9:60–71.
- Histed SN, Lindenberg ML, Mena E, Turkbey B, Choyke PL, Kurdziel KA. Review of functional/anatomical imaging in oncology. *Nucl Med Commun*. 2012;33:349–61.
- Dunet V, Pomoni A, Hottinger A, Nicod-Lalonde M, Prior JO. Performance of 18F-FET versus 18F-FDG-PET for the diagnosis and grading of brain tumors: systematic review and meta-analysis. *Neuro Oncol*. 2016;18:426–34.
- Chen W, et al. Imaging proliferation in brain tumors with 18F-FLT PET: comparison with 18F-FDG. *J Nucl Med*. 2005;46:945–52.
- Scott AM, et al. PET changes management and improves prognostic stratification in patients with recurrent colorectal cancer: results of a multicenter prospective study. *J Nucl Med*. 2008;49:1451–7.
- Kraeber-Bodere F, Bailly C, Chérel M, Chatal JF. ImmunoPET to help stratify patients for targeted therapies and to improve drug development. *Eur J Nucl Med Mol Imaging*. 2016;43:2166–8.
- Han S, Woo S, Kim YJ, Suh CH. Impact of (68)Ga-PSMA PET on the management of patients with prostate cancer: a systematic review and meta-analysis. *Eur Urol*. 2018;74:179–90.
- Götz I, Grosu AL. [(18)F]FET-PET imaging for treatment and response monitoring of radiation therapy in malignant glioma patients - a review. *Front Oncol*. 2013;3:104.
- Lee HS, et al. The development of 18F fluorothanatracer: A PET radiotracer for imaging poly (ADP-Ribose) polymerase-1. *Radiology: Imaging Cancer* 4, e210070 (2022).
- Young RJ, et al. Preclinical and first-in-human-brain-cancer applications of [18F]poly (ADP-ribose) polymerase inhibitor PET/MR. *Neuro-Oncology Advances* 2, (2020).
- Penning TD, et al. Discovery of the Poly(ADP-ribose) polymerase (PARP) inhibitor 2-[(R)-2-methylpyrrolidin-2-yl]-1H-benzimidazole-4-carboxamide (ABT-888) for the treatment of cancer. *J Med Chem*. 2009;52:514–23.
- Byers LA, et al. Veliparib in combination with carboplatin and etoposide in patients with treatment-naïve extensive-stage small cell lung cancer: a phase 2 randomized study. *Clin Cancer Res*. 2021;27:3884–95.
- Owonikoko TK, et al. Randomized phase II trial of cisplatin and etoposide in combination with veliparib or placebo for extensive-stage small-cell lung cancer: ECOG-ACRIN 2511 study. *J Clin Oncol*. 2019;37:222–9.
- Dieras V, et al. Veliparib with carboplatin and paclitaxel in BRCA-mutated advanced breast cancer (BROCADE3): a randomised, double-blind, placebo-controlled, phase 3 trial. *Lancet Oncol*. 2020;21:1269–82.
- Boussios S, et al. Veliparib in ovarian cancer: a new synthetically lethal therapeutic approach. *Invest New Drugs*. 2020;38:181–93.
- Reilly SW, et al. Synthesis and evaluation of an AZD2461 [(18)F] PET probe in non-human primates reveals the PARP-1 inhibitor to be non-blood-brain barrier penetrant. *Bioorg Chem*. 2019;83:242–9.
- de Gooijer MC, Buil LCM, Çitirikaya CH, Hermans J, Beijnen JH, van Tellingen O. ABCB1 attenuates the brain penetration of the PARP inhibitor AZD2461. *Mol Pharm*. 2018;15:5236–43.

27. Zeng H, Zhang H, Jang F, Zhao L, Zhang J. Molecular modeling studies on benzimidazole carboxamide derivatives as PARP-1 inhibitors using 3D-QSAR and docking. *Chem Biol Drug Des*. 2011;78:333–52.
28. Almahli H, et al. Development of novel synthesized phthalazinone-based PARP-1 inhibitors with apoptosis inducing mechanism in lung cancer. *Bioorg Chem*. 2018;77:443–56.
29. Wang H, et al. Discovery of pamiparib (BGB-290), a potent and selective poly (ADP-ribose) polymerase (PARP) inhibitor in clinical development. *J Med Chem*. 2020;63:15541–63.
30. Wilson AA, Jin L, Garcia A, DaSilva JN, Houle S. An admonition when measuring the lipophilicity of radiotracers using counting techniques. *Appl Radiat Isot*. 2001;54:203–8.
31. De Feyter HM, et al. A ketogenic diet increases transport and oxidation of ketone bodies in RG2 and 9L gliomas without affecting tumor growth. *Neuro Oncol*. 2016;18:1079–87.
32. Papp EA, Leergaard TB, Calabrese E, Johnson GA, Bjaalie JG. Waxholm space atlas of the Sprague Dawley rat brain. *Neuroimage*. 2014;97:374–86.
33. Baum E, et al. PET imaging evaluation of four sigma1 radiotracers in nonhuman primates. *J Nucl Med*. 2017;58:982–8.
34. Cai Z, et al. Synthesis and preclinical evaluation of an 18F-labeled synaptic vesicle glycoprotein 2A PET imaging probe: [18F]SynVesT-2. *ACS Chem Neurosci*. 2020;11:592–603.
35. Thorsell A-G, et al. Structural basis for potency and promiscuity in Poly(ADP-ribose) polymerase (PARP) and tankyrase inhibitors. *J Med Chem*. 2017;60:1262–71.
36. Rouleau M, Patel A, Hendzel MJ, Kaufmann SH, Poirier GG. PARP inhibition: PARP1 and beyond. *Nat Rev Cancer*. 2010;10:293–301.
37. Hitchcock SA. Structural modifications that alter the P-glycoprotein efflux properties of compounds. *J Med Chem*. 2012;55:4877–95.
38. Kolaczowski L, Barkalow J, Barnes DM, Haight A, Pritts W, Schellinger A. Synthesis of (R)-Boc-2-methylproline via a memory of chirality cyclization. application to the synthesis of veliparib, a poly(ADP-ribose) polymerase inhibitor. *The Journal of Organic Chemistry* 84, 4837–4845 (2019).
39. Rankovic Z. CNS drug design: balancing physicochemical properties for optimal brain exposure. *J Med Chem*. 2015;58:2584–608.
40. Niu J, et al. Parent-metabolite pharmacokinetic modeling and pharmacodynamics of veliparib (ABT-888), a PARP inhibitor, in patients with BRCA 1/2-mutated cancer or PARP-sensitive tumor types. *J Clin Pharmacol*. 2017;57:977–87.
41. Li X, Delzer J, Voorman R, de Moraes SM, Lao Y. Disposition and drug-drug interaction potential of veliparib (ABT-888), a novel and potent inhibitor of Poly(ADP-ribose) polymerase. *Drug Metab Dispos*. 2011;39:1161–9.
42. Lassen NA, et al. Benzodiazepine receptor quantification in vivo in humans using [11C]flumazenil and PET: application of the steady-state principle. *J Cereb Blood Flow Metab*. 1995;15:152–65.
43. Cunningham VJ, Rabiner EA, Slifstein M, Laruelle M, Gunn RN. Measuring drug occupancy in the absence of a reference region: the Lassen plot re-visited. *Journal of cerebral blood flow and metabolism: official journal of the International Society of Cerebral Blood Flow and Metabolism*. 2010;30:46–50.
44. Naganawa M, et al. Receptor occupancy of the  $\kappa$ -opioid antagonist LY2456302 measured with positron emission tomography and the novel radiotracer 11C-LY2795050. *J Pharmacol Exp Ther*. 2016;356:260–6.
45. Ferreira MT, Berger L, Rouleau M, Poirier GG. Assessment of PARP-1 distribution in tissues of cynomolgus monkeys. *J Histochem Cytochem*. 2020;68:413–35.
46. Tu Z, Chu W, Zhang J, Dence CS, Welch MJ, Mach RH. Synthesis and in vivo evaluation of [11C]PJ34, a potential radiotracer for imaging the role of PARP-1 in necrosis. *Nucl Med Biol*. 2005;32:437–43.
47. Reiner T, et al. Imaging therapeutic PARP inhibition in vivo through bioorthogonally developed companion imaging agents. *Neoplasia*. 2012;14:169–77.
48. Carlucci G, et al. Dual-modality optical/PET imaging of PARP1 in glioblastoma. *Mol Imaging Biol*. 2015;17:848–55.
49. Zhou D, et al. Synthesis, [(1)(8)F] radiolabeling, and evaluation of poly (ADP-ribose) polymerase-1 (PARP-1) inhibitors for in vivo imaging of PARP-1 using positron emission tomography. *Bioorg Med Chem*. 2014;22:1700–7.
50. Michel LS, et al. PET of poly (ADP-Ribose) polymerase activity in cancer: preclinical assessment and first in-human studies. *Radiology*. 2017;282:453–63.
51. Carney B, et al. Target engagement imaging of PARP inhibitors in small-cell lung cancer. *Nat Commun*. 2018;9:176.
52. Shuhendler AJ, et al. [(18)F]-SuPAR: a radiofluorinated probe for noninvasive imaging of DNA damage-dependent Poly(ADP-ribose) polymerase activity. *Bioconjug Chem*. 2019;30:1331–42.
53. Zhou D, et al. Radiosynthesis and evaluation of talazoparib and its derivatives as PARP-1-targeting agents. *Biomedicines* 9, (2021).
54. Pillie PG, Gay CM, Byers LA, O'Connor MJ, Yap TA. PARP inhibitors: extending benefit beyond BRCA-mutant cancers. *Clin Cancer Res*. 2019;25:3759–71.
55. Wang L, et al. PARP1 in carcinomas and PARP1 inhibitors as antineoplastic drugs. *Int J Mol Sci* 18, (2017).
56. Miknyoczki S, et al. The selective poly(ADP-ribose) polymerase-1(2) inhibitor, CEP-8983, increases the sensitivity of chemoresistant tumor cells to temozolomide and irinotecan but does not potentiate myelotoxicity. *Mol Cancer Ther*. 2007;6:2290–302.
57. Lammertsma AA, Hume SP. Simplified reference tissue model for PET receptor studies. *Neuroimage*. 1996;4:153–8.
58. Wu Y, Caron RE. Noise reduction in the simplified reference tissue model for neuroreceptor functional imaging. *J Cereb Blood Flow Metab*. 2002;22:1440–52.
59. Wiegand R, Wu J, Sha X, LoRusso P, Li J. Simultaneous determination of ABT-888, a poly (ADP-ribose) polymerase inhibitor, and its metabolite in human plasma by liquid chromatography/tandem mass spectrometry. *J Chromatogr B Analyt Technol Biomed Life Sci*. 2010;878:333–9.
60. Kikuchi R, et al. Prediction of clinical drug-drug interactions of veliparib (ABT-888) with human renal transporters (OAT1, OAT3, OCT2, MATE1, and MATE2K). *J Pharm Sci*. 2013;102:4426–32.
61. Carney B, et al. Non-invasive PET imaging of PARP1 expression in glioblastoma models. *Mol Imaging Biol*. 2016;18:386–92.
62. Donawho CK, et al. ABT-888, an orally active poly(ADP-ribose) polymerase inhibitor that potentiates DNA-damaging agents in preclinical tumor models. *Clin Cancer Res*. 2007;13:2728–37.
63. Kauppinen TM, Swanson RA. The role of poly(ADP-ribose) polymerase-1 in CNS disease. *Neuroscience*. 2007;145:1267–72.
64. Curtin NJ, Szabo C. Poly(ADP-ribose) polymerase inhibition: past, present and future. *Nat Rev Drug Discovery*. 2020;19:711–36.
65. Olsen AL, Feany MB. PARP inhibitors and parkinson's disease. *N Engl J Med*. 2019;380:492–4.
66. Lengyel-Zhand Z, Puentes LN, Mach RH. PARKinson's: From cellular mechanisms to potential therapeutics. *Pharmacol Ther*. 2022;230: 107968.

**Publisher's note** Springer Nature remains neutral with regard to jurisdictional claims in published maps and institutional affiliations.

Springer Nature or its licensor (e.g. a society or other partner) holds exclusive rights to this article under a publishing agreement with the author(s) or other rightsholder(s); author self-archiving of the accepted manuscript version of this article is solely governed by the terms of such publishing agreement and applicable law.

## Authors and Affiliations

Baosheng Chen<sup>1</sup> · Devi Prasan Ojha<sup>1</sup> · Takuya Toyonaga<sup>1</sup> · Jie Tong<sup>1</sup> · Richard Pracitto<sup>1</sup> · Monique A. Thomas<sup>2</sup> · Michael Liu<sup>1</sup> · Michael Kapinos<sup>1</sup> · Li Zhang<sup>1</sup> · Ming-Qiang Zheng<sup>1</sup> · Daniel Holden<sup>1</sup> · Krista Fowles<sup>1</sup> · Jim Ropchan<sup>1</sup> · Nabeel Nabulsi<sup>1</sup> · Henk De Feyter<sup>2</sup> · Richard E. Carson<sup>1</sup> · Yiyun Huang<sup>1</sup> · Zhengxin Cai<sup>1</sup> 

<sup>1</sup> Yale PET Center, Department of Radiology and Biomedical Imaging, Yale University, 801 Howard Avenue, PO Box 208048, New Haven, CT 06520-8048, USA

<sup>2</sup> Magnetic Resonance Research Center, Department of Radiology and Biomedical Imaging, Yale University, New Haven, CT, USA